CHALMERS
UNIVERSITY OF TECHNOLOGY

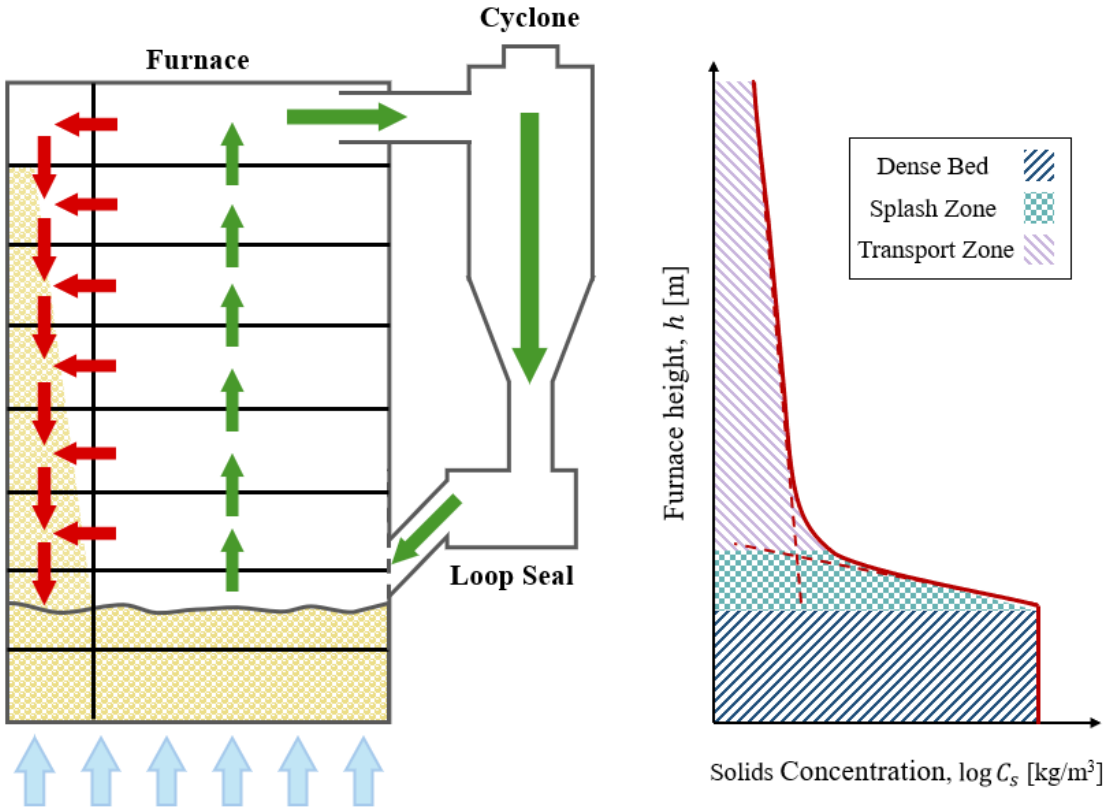

1.5D Modeling of a Biomass-Fired Circulating Fluidized Bed Boiler

JUAN MANUEL RUBIO VANEGAS

DEPARTMENT OF ENVIRONMENTAL AND ENERGY SCIENCES

CHALMERS UNIVERSITY OF TECHNOLOGY
Gothenburg, Sweden 2026
www.chalmers.se

Master's thesis 2026

1.5D Modeling of a Biomass-Fired Circulating Fluidized Bed Boiler

JUAN MANUEL RUBIO VANEGAS

CHALMERS
UNIVERSITY OF TECHNOLOGY

Department of Environmental and Energy Sciences
Division of Energy Technology
Fluidization Research Group
Chalmers University of Technology
Gothenburg, Sweden 2026

1.5D Modeling of a Biomass-Fired Circulating Fluidized Bed Boiler
JUAN MANUEL RUBIO VANEGAS

Supervisor: David Pallarès
Examiner: David Pallarès

Master's Thesis 2026
Department of Environmental and Energy Sciences
Division of Energy Technology
Fluidization Research Group
Chalmers University of Technology
SE-412 96 Gothenburg
Telephone +46 76 181 6657

Cover: Reduced-order visualization of a circulating fluidized bed (CFB) boiler, together with the vertical solids concentration profile.

Typeset in LaTeX
Printed by Chalmers Reproservice
Gothenburg, Sweden 2026

1.5D Modeling of a Biomass-Fired Circulating Fluidized Bed Boiler
JUAN MANUEL RUBIO VANEGAS
Department of Environmental and Energy Sciences
Chalmers University of Technology

Abstract

Biomass-fired circulating fluidized bed (CFB) boilers are widely used because of their fuel flexibility and efficient combustion with reduced emissions. Accurate prediction of the gas-solid flow patterns and fuel conversion behavior is important for design, optimization, and operational studies. High-fidelity, detailed modeling approaches, such as computational fluid dynamics (CFD), may be computationally expensive. On the other hand, simplified, reduced-order models can provide less detailed predictions at a lower computational cost.

The objective of this work was to develop a transient semi-empirical 1.5D model capable of predicting the solid hydrodynamics and fuel conversion behavior of large-scale biomass-fired CFB units. The model combines vertical discretization of the furnace with a radial core-annulus structure to represent the main fluid-dynamical structures. The hydrodynamic behavior was described through transient mass balances, employing empirical and semi-empirical correlations to describe the solids entrainment, lateral solids transport, and back-mixing phenomena. Fuel conversion was incorporated through source terms coupled to the mass balances, representing the drying, devolatilisation, and char combustion of the fuel particles. The resulting system of differential equations was solved numerically and validated against experimental measurements of representative large-scale units.

The model captured the expected hydrodynamic trends and predicted vertical solids concentration profiles with reasonable agreement with fluidization physics and the experimental data. Sensitivity analyses showed strong dependence on the lateral transport and operating conditions, such as the gas velocity. Fuel conversion simulations demonstrated physically consistent evolution of particle properties and conversion stages. The model achieved these results, preserving a relatively low computational cost, requiring less than 450 seconds to simulate over 2000 seconds of boiler operation. The developed model provides an efficient framework for analyzing industrial CFB operation, and can support future extensions involving gas species transport, more robust hydrodynamic considerations, and heat transfer.

Keywords: fluidization, circulating fluidized bed, combustion, semi-empirical, modeling, transport, biomass, hydrodynamics, conversion, boiler.

Acknowledgements

"All that happens has been fated by the Whole
from the beginning and spun for your own destiny."

— *Marcus Aurelius*

If someone had told me five years ago that I would be writing a Master's Thesis in Sweden, I wouldn't have been able to believe it. Despite repeated attempts, I find it very difficult to define the precise moment that began the spiraling of events that brought me here, the flap of a butterfly's wings that started the hurricane. The only thing I am completely sure about is that I would not be here today if it were not for my mom. Mamita linda, I am unable to put into words the level of admiration I have for you and your dedication to everything you do. It is because of you that I studied in Bogota's best school, which got me admitted into Colombia's best university, which got me here, to Sweden, a destination out of our plans, but that has meant and will mean so much for our future. You are my butterfly effect, mom. You are the reason I have come so far.

I am also fortunate enough to have a lot of people to dedicate this thesis to. To my entire family, my godmother, my godsons, I love you, and I have kept you close to my heart. To my grandmother, the toughest woman ever, and my uncle, the man I wished I had known for a longer time, I know you were with me today and always. To Ed, my extra, the father I was not expecting, for always believing in me, being proud of me, sharing my triumphs, loving my mom, and for teaching me how to install a Rheem water heater. You played a huge part in this adventure. You never doubted me, even when I did. To Pacho Duarte, the man who I thought was training me for basketball, but who ended up training me for life. To my Dad, whom I love deeply.

To David, Carolina, Felicia, and Jia, the best supervisors I have ever had. Thank you for always driving me to give the best of myself, for never doubting that I was capable of big things. It has been almost a year since I joined the Fluidization research group, and it has been one of the best decisions I have ever made. To Jing, Azka, Farha, Philip, Victor, and Rustan, for being welcoming and warm, and for all the help you have given me in all my projects.

To Preci, Poche, and David, whom I proudly call my brothers despite not sharing blood, who have been there since the beginning and never left, for sharing so many memories and laughter. I love you, guys. To Camilo, Guillermo, and my UNAL people, who have known the struggle, who have been there since 2018, and have always supported my decisions and treated me like family.

To Murilo and Hailan, who appeared in my life when I most needed them, who never said no to a coffee, with whom we shared highs and lows. I am lucky to have you as my friends. To Mariana, my Colombia in Sweden, together since day 1, living the same dream, pushing beyond our limits, happy for each other's success, lifting

each other up in our worst moments. Somehow, I cannot think of a single time that we did any activity without food being involved somehow. Looking forward to calling you Doctor in 5 years. To Tosh, Ken, Daniel, and Johannes, for adopting me into your amazing friend group. Counting the days for the next group vacation. To Mafe, Karenn, Saúl, Alonso, and Poncho, who arrived one year later but who have meant so much, and have given me reasons to smile every time I see them.

To my fellow Energy Division MSc. Thesis students and colleagues. To Ellen, Adam, Malte, Linnea, Simon, Henrik, and Giulio for keeping the working days full of drama, and inviting me to have a drink with them every chance they got. To Felix, whom I proudly call my first Swedish friend, for believing in me. To Benjamin, Hermann, Noah, Alex, and Leandro, the OG Division working students, for being there when it all started.

To all the professors that I have had in my life. You taught me everything I know.

And finally, to myself. The result of years of preparation, hard work, and dedication. It has been an intense path, but I would not change a single thing about it.

Juan Manuel Rubio Vanegas, Gothenburg, May 2026

Acknowledgement of AI Use

AI Software - ChatGPT and Grammarly - has been used in this work for grammar and syntax checking in the writing of the thesis. Additionally, ChatGPT aided in the elaboration of post-processing plotting routines, in the profiling activities of the code to analyze performance statistics, and to suggest solver configurations to improve overall code performance.

Contents

List of Acronyms

BDF	Backward Differentiation Formula
CFB	Circulating fluidized bed
CFD	Computational fluid dynamics
FB	Fluidized bed
KC	Kraftcentralen
ODE	Ordinary differential equation
PSD	Particle size distribution

List of Symbols

Symbol	Description	Unit
C_{char}	Concentration of char	kg/m^3
C_{dry}	Concentration of dry biomass	kg/m^3
C_{wet}	Concentration of wet biomass	kg/m^3
C_s	Solids mass concentration	kg/m^3
D_i	Dispersion coefficient	m^2/s
D	Characteristic length for solids separation efficiency	m
D_0	Furnace depth	m
D_h	Dispersion coefficient for horizontal/lateral mixing	m^2/s
$\varnothing_h$	Equivalent (hydraulic) diameter	m
$D_{\mathbf{bot}}$	Lower-face diffusive transport term	kg/s
$D_{\mathbf{lat}}$	Lateral diffusive transport term	kg/s
$D_{\mathbf{top}}$	Upper-face diffusive transport term	kg/s
d_p	Particle diameter	m
d_p^*	Dimensionless particle diameter	–
D_v	Dispersion coefficient for vertical/axial mixing	m^2/s
g	Gravitational acceleration	m/s^2
$G_{s,e}$	Solids entrainment flux	kg/m^2s
$G_{s,e}^*$	Dimensionless solids entrainment flux	–
$h_{\mathbf{coarse}}$	Height of coarse vertical layers in the computational mesh	–
$H_{\mathbf{outlet}}$	Cyclone duct height	m
$h_{\mathbf{fine}}$	Height of fine vertical layers in the computational mesh	–
H_0	Furnace height	m
$H_{\mathbf{at}}$	Distance from the roof of the furnace to the top of the outlet duct	m
H_{sat}	Saturation height	m
$I(t, \tau_i)$	Injection curve function	–

$J_{\mathbf{bot}}$	Lower-face convective transport term	kg/s
$J_{\mathbf{lat}}$	Lateral convective transport term	kg/s
$J_{\mathbf{top}}$	Upper-face convective transport term	kg/s
k	Mass transfer coefficient	m/s
$\dot{m}_{ann,fb}$	Solids downflow in the annulus region of the transport zone	kg/s
$\dot{m}_{diff}$	Diffusive mass transfer	kg/s
$\dot{m}_{diff,h}$	Horizontal diffusive mass transfer	kg/s
$\dot{m}_{diff,v}$	Vertical diffusive mass transfer	kg/s
$\dot{m}_{fuel,in}$	Fuel mass flow into the furnace	kg/s
$\dot{m}_{lat}$	Lateral solids mass flow	kg/s
$\dot{m}_{lat,top}$	Lateral solids mass flow at the top of the boiler	kg/s
$\dot{m}_{\mathbf{net}}$	Net mass transport in a computational cell	kg/s
$\dot{m}_{core,fb}$	Solids upflow in the core region of the transport zone	kg/s
$\dot{m}_{s,e}$	Solids entrainment mass flow	kg/s
$n_{\mathbf{coarse}}$	Number of coarse vertical layers in the computational mesh	–
$n_{\mathbf{fine}}$	Number of fine vertical layers in the computational mesh	–
R_i	Injection rate	kg/s, m/s
R_h	Coarse-to-fine layer height ratio	–
$S_{\mathbf{outlet}}$	Cyclone duct cross-sectional area	m^2
S_0	Riser cross-sectional area	m^2
$S_{\mathbf{c}}$	Fuel conversion source term	kg/s
$S_{\mathbf{f}}$	Solids feeding source term	kg/s
St	Stokes number	–
t_0	Injection start time	s
t_{wall}	Wall layer thickness	m
u_g	Fluidization velocity	m/s
$u_{g,\mathbf{PA}}$	Primary air velocity	m/s
$u_{g,\mathbf{SA}}$	Secondary air velocity	m/s
u_t	Particle terminal velocity	m/s
u_t^*	Dimensionless terminal velocity	–
u_w	Velocity at the wall layers	m/s
V	Volume	m^3
$\dot{V}$	Volumetric flow for convection loop in the dense bed	m^3/s

w	Mass fraction of a solid	–
$W_{\mathbf{outlet}}$	Cyclone duct width	m
L_0	Furnace width	m
$X_{\mathbf{char}}$	Fuel fixed carbon content	–
$X_{\mathbf{moist}}$	Fuel moisture content	–
$X_{\mathbf{vol}}$	Fuel volatiles content	–

Greek Symbols

Symbol	Description	Unit
$\Delta C_{s,h}$	Horizontal concentration difference	kg/m^3
$\Delta C_{s,v}$	Vertical concentration difference	kg/m^3
δ	Dense bed tracking threshold	–
$\varepsilon_{\mathbf{layer}}$	Local solids fraction in each layer	–
ε_s	Solids fraction	–
ε_g	Voidage or gas fraction	–
η_{ss}	Solids separation efficiency at the exit zone	–
μ_g	Gas viscosity	Pa · s
ϕ	Particle sphericity	–
ρ_g	Gas density	kg/m^3
ρ_s	Solids particle density	kg/m^3
τ_1	Drying characteristic time	s
τ_2	Devolatilization characteristic time	s
τ_3	Char combustion characteristic time	s
τ_i	Injection curve characteristic time	s
ξ	Relative gas velocity	–

List of Figures

List of Tables

1

Introduction

1.1 Energy Context and Relevance of Fluidized Bed Systems

As the energy transition progresses, fossil-fuel-dependent industrial sectors gradually move toward fully electrified configurations. The progressive reduction of fossil-based electricity generation, the increasing variability of energy systems introduced by the growing penetration of renewable power sources, and the need to ensure net-negative CO_2 emissions to the atmosphere create a demand for efficient and flexible thermal power systems capable of supplying electricity with low environmental impact.

Fluidized bed (FB) technology has undergone decades of development. Particularly, advances in gas-solid FB systems have led to their wide application in the energy and power industries [1]. In these reactors, a bed of solid particles develops fluid-like behavior when a gas is injected at the bottom, exhibiting high mixing rates in both the solid and gas phases, and resulting in high mass and heat transfer rates [2]. Furthermore, the large inventory of bed solids provides significant thermal capacity, promoting homogeneous furnace temperatures that increase efficiency and reduce emissions during combustion [2]. These characteristics, together with fuel flexibility and the capability for in-bed emission capture [3], make FB technologies highly attractive for future energy systems.

Circulating fluidized beds (CFB) are a type of FB reactor in which the use of higher gas velocities to intensify the combustion process by increasing the energy release density (W/m2) requires the implementation of a solids recirculation system, as stronger gas flows introduced particle entrainment of the bed material [3]. The high thermal mixing and inertia of CFBs [3], together with their flexibility and efficiency, make them highly attractive units for biomass combustion and gasification [4]. Biomass fuels are an important component of climate mitigation strategies, as they are potential carbon-neutral, renewable sources for heat and electricity generation [4]. Thus, biomass-fired CFB systems are of considerable environmental and industrial interest due to their potential contribution to the global reduction of greenhouse gas emissions and energy transition [5].

1.2 Modeling of CFB Boilers

1.2.1 Role of Modeling in Fluidized Bed Systems

FB systems are applied in several processes and involve a wide variety of complex phenomena that often require dedicated modeling [6]. Experimental techniques used to characterize the FB behavior have undergone significant development in recent years, but they still exhibit limited temporal and spatial resolution in the acquired data [1]. Thus, modeling efforts focus on providing a deeper understanding of FB systems through the characterization of the fluid dynamics, chemistry, and heat transfer, with fluid-dynamic modeling having a central role due to its strong influence on the other fields [7]. These models can generally be classified as either macroscopic, based on empirical and semi-empirical formulations (i.e., relying on experimental data to describe the flow fields instead of solving the momentum equations [3]), or mechanistic models using computational fluid dynamics (CFD) [7]. Macroscopic modeling is very practical as it seeks to maintain high physical agreement with the fluidization phenomena, while keeping relatively low computational cost [7]. However, its dependence on experimental data may restrict its applicability to similar conditions to those used in the development of its semiempirical closures [3]. Therefore, it is of interest to develop generic FB models that apply to a wide range of operating conditions, geometries, and applications, while remaining physically consistent and computationally efficient.

1.2.2 Challenges in CFB Modeling

CFB modeling involves the consideration of multiple underlying phenomena.In particular, the gas-solid flow in CFB units is highly complex [1]. Time- and space-dependent flow structures throughout the furnace, and may vary considerably with operating conditions and geometry [8]. As described in Chapter 2, three main flow regions are typically identified in large-scale CFB furnace: a dense region located at the bottom, followed by splash and transport regions directly above it [3]. Each of these regions, together with the solids recirculation loop, exhibits distinct dynamic behavior and requires specific formulations. Consequently, different modeling strategies can be adopted for CFB systems, depending on the desired level of information and detail.

1.2.3 Modeling Strategies for CFB Boilers

Model complexity can range from global formulations (0D models) to high-spatial-resolution approaches (2D and 3D models) [6]. As illustrated in Figure 1.1, increasing the spatial resolution of a model provides a higher level of detail in the predictions of the system's behavior, at the expense of increased computational cost. Therefore, the selection of the modeling approach depends on balancing computational efficiency with the desired prediction accuracy and detail. The main categories for modeling strategies are described below.

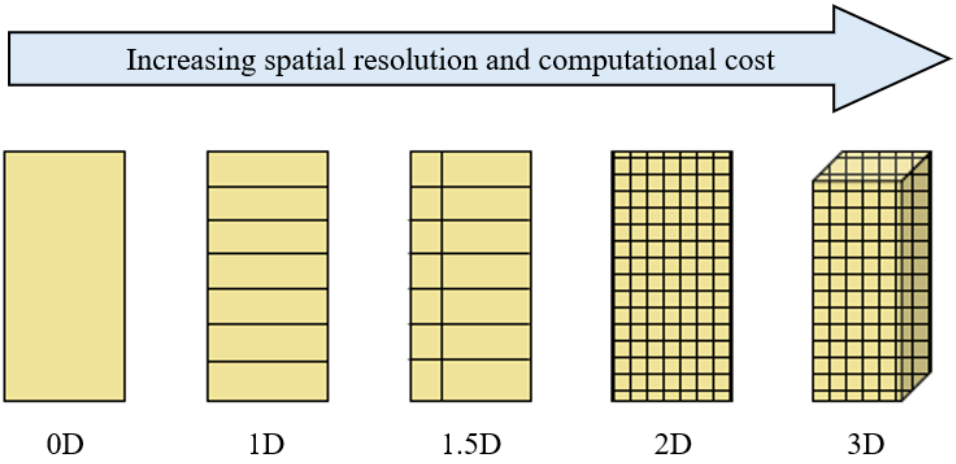

Figure 1.1: Schematic of increasing model dimensionality, from global 0D representations to 3D models.

1.2.3.1 0D Models

Global or 0D models (also known as black box models) present an overall description of a CFB system without spatial discretization, based mainly on on-site experimental measurements. These models can provide useful predictions of representative state variables such as the solids concentration in the boiler and the heat transfer in the furnace [9]. However, the dependence on experimental data limits their validity to the operating conditions and boiler geometry in which the measurements were taken [9].

1.2.3.2 1-1.5D Models

1D models make use of discrete cells to describe the vertical gradients of different state variables in CFB units, such as gas and solid concentrations or temperature [6]. These approaches typically employ empirical and semi-empirical correlations to describe hydrodynamic behavior such as pressure drop and solids circulation throughout the furnace height [10]. The development of 1.5D models gained relevance after studies in the 80's confirmed the lateral distinction of a core upward flow and an annulus/wall layer downward flow [6]. As indicated in Figure 1.1, 1.5D models represent an intermediate approach between 1D and 2D models, representing radial variations in flow structures together with a complete vertical discretization of the furnace. Hannes [6] made use of this approach to preserve a relatively simple model formulation, while achieving a good level of spatial resolution at a lower computational cost than CFD simulations at the time. However, the author also recognized that more comprehensive CFB models could be achieved through CFD simulations.

1.2.3.3 2D–3D Models

2D/3D models achieve higher spatial resolution through detailed discretization of the system. The complexity of these models is considerably higher and can vary

based on the computational mesh resolution. More detailed spatial descriptions of the system provide more information about the flows, such as local erosion sites, accumulation points, or hot spots [6], but incur higher computational costs [8]. Different strategies can be applied to reduce the computational cost, as described by Yang et al. [10], reducing computational time by using the results of semi-empirical 1D models as initial conditions for 3D CFD simulations of CFB systems. Nevertheless, the applicability and predictive performance are still conditioned by the availability of computational resources.

1.3 Aim and Objectives

The purpose of this MSc Thesis is to develop a comprehensive 1.5D model of a Biomass-Fired Circulating Fluidized Bed (CFB) boiler that can represent the operational behavior and yield values for key performance indicators like solids concentration distributions from a set of inlet parameters comprising the operating conditions of interest, such as fluidization gas speed, bed material, and geometry. To test the model's accuracy and effectiveness at representing real operating behavior, as well as its generalizability, it will be validated with data from two industrial-scale units: a large-scale CHP unit owned by the Danish utility company HOFOR and Chalmers' 12 MW boiler.

The main objectives of this work are to:

- Construct a robust reduced-order model of a large-scale biomass-fired CFB boiler capable of capturing the main characteristics of industrial operation.
- Achieve a thorough representation of relevant physical phenomena such as gas-solid interactions and reaction kinetics, through the use of empirical correlations.
- Perform a model validation utilizing the provided industrial operation data from HOFOR and Chalmers to corroborate the approximation effectiveness and representativeness of the results.
- Assess the limitations and future improvements that the model could undergo to achieve a higher level of accuracy and validity.

1.4 Scope of the Present Work

The modeling work in this thesis is restricted to large-scale biomass-fired CFB units operating under industrially relevant conditions and using bed material particles within the Geldart B classification. The developed model includes a detailed representation of the gas-solid flow in the vertical direction, while accounting for radial flow variations through a core-annulus formulation. A constant temperature of 800°C is taken as a model input, as the heat balance is not closed in the present work. In addition, simplified formulations are included to represent the effects of secondary air injection and fuel conversion.

2

Theory

The focus of this chapter is to summarize the underlying phenomena that govern the gas-solids flow and fuel conversion of CFB units, and to state the expressions and assumptions used in their modeling. The structure and details, including inputs/outputs and balances, of the model developed in this work are presented in Chapter 3.

2.1 General Fluidization Definitions

2.1.1 Particle Terminal Velocity

The terminal velocity plays a key role in the solids transport in the riser and represents the velocity at which the drag force balances the net gravitational force acting on a particle [11]. In practice, the solids inventory of CFBs consists of a particle size distribution (PSD). Particles within the distribution can have different sizes and thereby terminal velocities (u_t). The terminal velocity is calculated by Grace et al.[11] using the dimensionless particle diameter, d_p^*, and the dimensionless terminal velocity, u_t^*, given by Equation 2.1 and Equation 2.2, respectively:

$$d_p^* = d_p \left(\frac{\rho_g g(\rho_s - \rho_g)}{\mu_g^2} \right)^{1/3} \tag{2.1}$$

$$u_t^* = u_t \left(\frac{\rho_g^2}{\mu_g g(\rho_s - \rho_g)} \right)^{1/3} \tag{2.2}$$

Furthermore, the dimensionless terminal velocity can be correlated through sphericity to the dimensionless particle diameter, yielding Equation 2.3, which is valid for $0.5 < \phi < 1$ [11]:

$$u_t^* = \left[\frac{18}{d_p^{*2}} + \frac{2.3348 - 1.7439\phi}{d_p^{*0.5}} \right]^{-1} \tag{2.3}$$

The above correlations are adopted throughout this work and are formulated for a single particle suspended in a fluid. The model could be further refined by incorporating terminal velocity correlations developed for solids suspensions, such as that of Win et al [12], which account for interparticle effects and provide more realistic estimates of particle motion inside particle suspensions.

2.1.2 Geldart Classification of Particles

Observations of the fluidization characteristics of different solids allowed David Geldart to classify particle behavior into 4 distinct groups [13]. Ordered by increasing particle size, these are: **Group C** (cohesive, or very fine powders); **Group A** (aeratable particles that fluidize easily at low gas velocities); **Group B** (sand-like particles exhibiting vigorous bubbling behavior); and **Group D** (coarse, spoutable particles) [14]. In industrial gas–solid systems, particularly in CFBs, Group B particles are most commonly employed as bed material [15]. When particles in this group fluidize with velocities exceeding the minimum fluidization velocity, the development of the bubbling regime facilitates efficient gas-solid mixing and rapid mass transfer, making Group B particles widely used in combustion and catalytic applications [16].

The present modeling work is restricted to Group B particles, as it relies on correlations and assumptions primarily developed and validated for large-scale CFB units operating with such solids. This ensures consistency and a more accurate reflection of the typical operating conditions of industrial CFBs.

2.1.3 Voidage and Solids Fraction

The flow in the furnace is composed of both a solid and a gas phase. It is necessary to define the voidage, ε_g, as the fraction of the local volume occupied by gas phase [11]. The corresponding solids fraction, ε_s, is given by Equation 2.4.

$$\varepsilon_s = 1 - \varepsilon_g \tag{2.4}$$

For a polydisperse solids mixture with constant particle density, the total solids fraction can be expressed as the sum of the individual contributions from each particle size class, as shown in Equation 2.5.

$$\varepsilon_s = \sum_i \varepsilon_{s_i} \tag{2.5}$$

If the total solids fraction and the mass fractions, w, obtained from a PSD are known, the individual solids fractions can be approximated as:

$$\varepsilon_{s_i} = w_i \varepsilon_s \tag{2.6}$$

This formulation assumes uniform particle density; modifications are required if density varies across size classes. Under this assumption, the mass concentration of particles of size i, C_s, is defined as Equation 2.7.

$$C_{s_i} = \rho_s \varepsilon_{s_i} \tag{2.7}$$

2.2 Gas-solids Flow in CFB Boilers

The injection of primary at the bottom of the riser establishes a gas-solid flow that evolves along the height of the furnace [17]. This evolution establishes three characteristic flow zones (illustrated in Figure 2.1):

- a **dense bed** zone at the bottom, where particles undergo continuous upward and downward motion due to bubble wake [18], leading to solid clusters being thrown up from the bed following bubble eruption [17].
- a **splash zone**, where the ballistic movement of the incoming solids clusters creates intense back-mixing toward the dense bed [19].
- a **transport zone**, where a more dispersed solids phase experiences less back-mixing. However, particles moving upwards tend to migrate to the wall layers and then flow downward, creating a core-annulus structure [17].

The splash and transport zone make up the freeboard, which occupies most of the riser height.

The formation of a dense bed is desirable for solid fuel combustion, as it promotes fuel mixing across the furnace cross-section [17]. Maintaining the solids inventory in the furnace requires continuous recirculation of the solids elutriated from the riser. A fraction of the solids entrained to the top of the riser exits to the cyclone carried by the flue gas [19]. Inside the cyclone (or cyclones, as larger units can have more than one), finer particles and gas are separated from the circulation loop and enter a convection pass to extract heat [17]. Heavier particles drop to a particle seal (typically a loop seal as shown in Figure 2.1) which operates as a bubbling bed moving solid particles back to the furnace bottom and feeds the solids back to the lower part of the furnace [7].

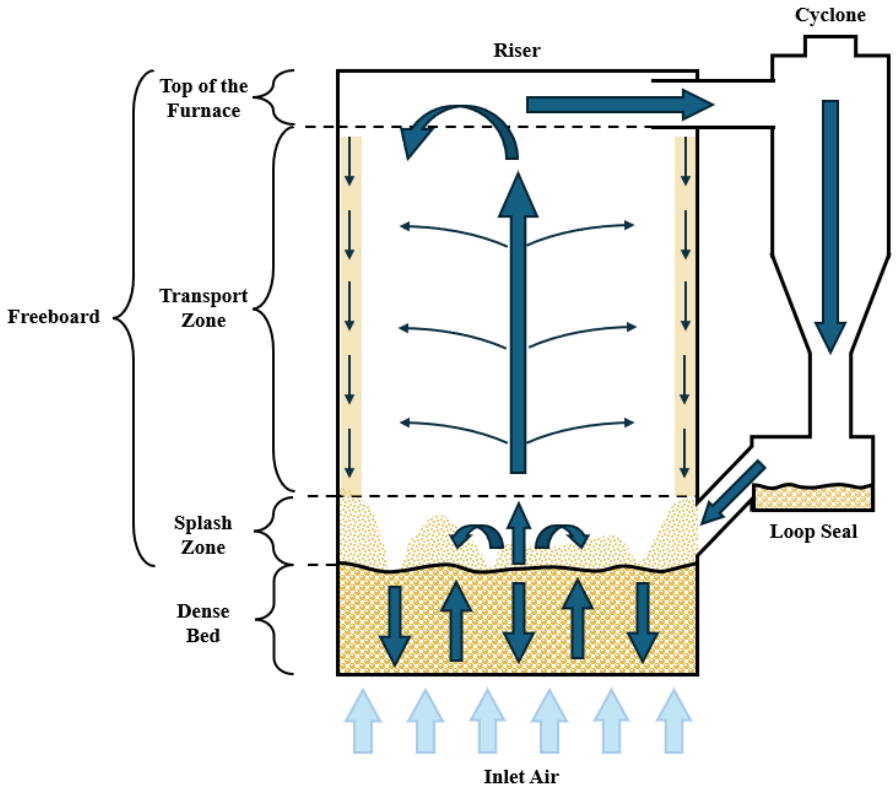

Figure 2.1: Fluid-dynamical regions in a CFB boiler

Previous studies of both industrial and laboratory-scale CFB units have allowed

for detailed mathematical descriptions of the flow zones mentioned earlier. The descriptions and correlations applied in the present work are included in the following sections, with their corresponding constraints and assumptions.

2.2.1 Dense Bed Zone

Johnsson et al. [20] defined the dense bed as the region where the pressure drop is constant with height, implying constant bed voidage and solids concentration. In industrial CFB units, the control system of the circulation loop aims to maintain a constant pressure drop by adjusting the bed inventory [21], making the dense bed height an important operational indicator. The dense bed height is strongly influenced by the fluidization gas velocity, u_g. Increasing u_g enhances solids entrainment, thereby reducing solids hold-up in the lower region. Djerf et al. [22] showed that, at sufficiently high gas velocities, the dense bed can be completely depleted. This has a direct effect on solids entrainment and the existence of the splash zone.

2.2.1.1 Solids Mixing

Solids mixing inside the dense bed is primarily driven by bubble motion [23]. Figure 2.2 illustrates the main mixing mechanisms that can be found inside the dense bed. In CFBs, bubble motion creates toroidal circulation paths, known as gulf streaming, in which the bed material rises in the central region of the structure and descends along its outer boundaries [9]. As a bubble rises, nearby solid particles are drawn into its wake, contributing to lateral mixing. Simultaneously, the bubbles push bed material upward, contributing to axial mixing. Upon reaching the bed surface, bubble eruption ejects clusters of particles into the freeboard, some of which fall back to the bed while others get entrained. In addition, neighboring bubble interactions and coalescence can further enhance the lateral mixing of solids in the bed [23]. This solid flow ultimately drags the fuel particles. The mixing of fuel inside the bed has a direct effect on residence times and conversion, with immersed fuel particles experiencing higher heat transfer rates than those floating or entrained in the freeboard [9].

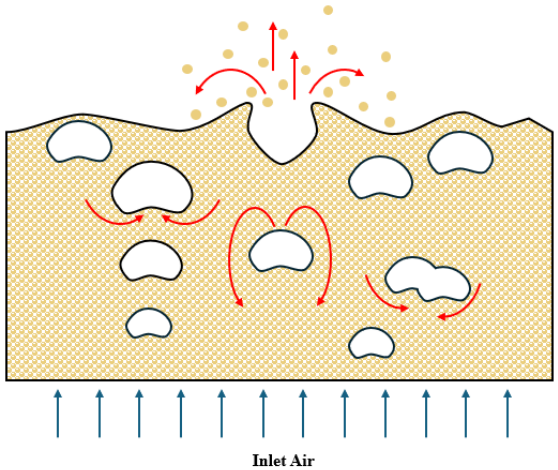

Figure 2.2: Schematic of solids mixing inside the dense bed due to bubble motion

All of the mechanisms described previously are dominated by the fluctuating behavior of the bubbling flow [24]. A common modeling approach is to group the mechanisms and describe the overall solids mixing through a single diffusion equation, as shown by Equation 2.8:

$$\frac{\partial C_s}{\partial t} = \frac{\partial C_s}{\partial x} D_x \left(\frac{\partial C_s}{\partial x} \right) + \frac{\partial C_s}{\partial y} D_y \left(\frac{\partial C_s}{\partial y} \right) + \frac{\partial C_s}{\partial z} D_z \left(\frac{\partial C_s}{\partial z} \right) \tag{2.8}$$

where C_s is the mass concentration and D_i are the dispersion coefficients in each spatial direction. For the modeling of the dense bed zone in this work, the equation is simplified assuming isotropic lateral mixing in the horizontal plane. Applying the Divergence theorem, the second-order differential equation can be written as a flux through an area such that the diffusive mass transfer, $\dot{m}_{diff}$, can be expressed as:

$$\dot{m}_{diff} = \dot{m}_{diff,h} + \dot{m}_{diff,v} = \frac{D_h}{\Delta x} A_{lat} \Delta C_{s,h} + \frac{D_v}{\Delta z} A_v \Delta C_{s,v} \tag{2.9}$$

where $\Delta C_{s,h}$ and $\Delta C_{s,v}$ represent the concentration differences between adjacent cells in both directions. More details on how the diffusive transport terms are shown in Chapter 3.

The dispersion coefficients account for both the convective and diffusive transport, with D_h considered constant in the horizontal plane, assuming an even distribution of the primary air gas nozzles in the cross section [24]. D_v typically takes values between 0.1 and 1 m^2/s, while D_h ranges between 0.01 and 10 m^2/s [25]. In the present work, the value of D_v is selected within the reported interval based on model performance and convenience. However, the value of D_h is chosen to be a very big number (i.e. 10^{10}) to allow for infinitely fast horizontal solids mixing in the dense bed, keeping the concentration in both cells of any horizontal plane the same. Uneven horizontal mixing within this zone would create local variations in the solids concentration, leading to spatially uneven bed voidage and pressure drop, deviating from the characteristic dense bed definition.

2.2.2 Freeboard Zone

As illustrated in Figure 2.1, the freeboard is the region extending from the dense bed surface to the top of the boiler [11]. Within this region, the solids concentration decays exponentially with height, combining the effects of solids back-mixing and entrainment. This decay is more pronounced within the splashing zone [26], as evidenced in Figure 2.3. In a logarithmic solids concentration profile, the splash and transport zones exhibit approximately constant slopes, with the splash zone showing a steeper decline due to a faster decrease in concentration. The solids concentration profile can be modified depending on the distribution of primary and secondary air injections. Although an increase in gas velocity above the secondary air injection level could be expected to reduce the solids concentration, experimental observations show that secondary air may instead increase the concentration by entraining particles that would have otherwise been back-mixed toward the dense region, to higher elevations in the furnace [27].

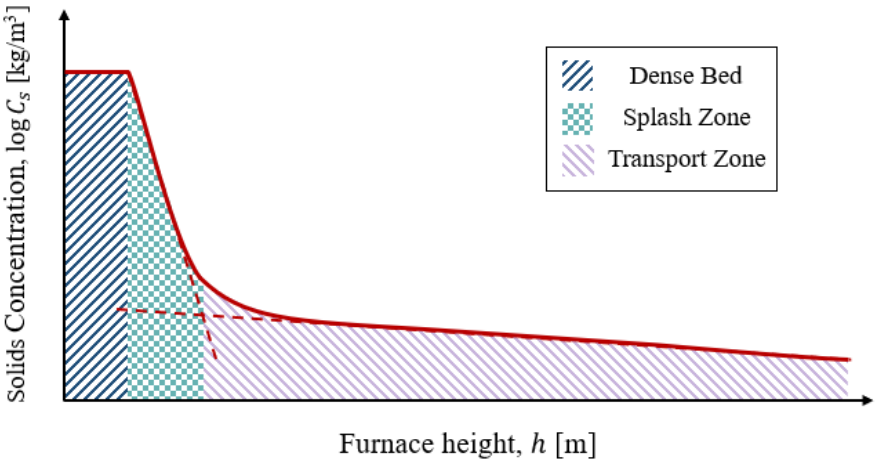

Figure 2.3: Typical logarithmic solids concentration profile, inspired by those built by Djerf et al. [22]

The following sections describe in detail the two zones that make up the freeboard, together with the main simplifications and assumptions used in the present work.

2.2.2.1 Splash Zone

The existence of the splash zone is conditioned by the presence of a dense bed at the bottom of the furnace. The splash zone is formed by the ejection of solid clusters from the dense bed surface by bubble eruptions. The clusters adopt a ballistic trajectory, during which some particles detach and are dragged upwards by the gas [26]. These dispersed particles leave the splashing zone and enter the transport zone. The flux of particles leaving the dense bed and splashing zone regions, and entering the transport zone is hereby defined as the solids entrainment [26].

Studies on the solids entrainment rates in large-scale units are limited, primarily due to the need for high spatial resolution in the concentration profiles. One notable contribution is the work of Djerf et al. [26], who combined experimental data from both industrial- and laboratory-scale CFB units operating with Geldart B particles with Monte Carlo simulations of ballistic particle trajectories. This enabled the quantification of the decay coefficients for concentration and the development of a comprehensive model for the solids entrainment flux, which depends on the gas and particle terminal velocity. To compare different operation conditions, the authors introduced the dimensionless solids entrainment flux, defined as:

$$G^*_{s,e} = \frac{G_{s,e}}{\rho_s u_g} \tag{2.10}$$

In turn, $G^*_{s,e}$ was correlated to experimental data, resulting in:

$$G^*_{s,e} = 0.0054(\xi - 1)^2, \text{ with } \xi = \frac{u_g}{u_t} \tag{2.11}$$

The entrainment mass flow, $\dot{m}_{s,e}$, can be defined by combining Equation 2.10 and Equation 2.11, yielding:

$$\dot{m}_{s,e} = \rho_s u_g G^*_{s,e} A = 0.0054 \rho_s u_g A (\xi - 1)^2 \tag{2.12}$$

In the present work, the splash zone is not explicitly resolved as a physical region within the computational domain. Instead, Equation 2.12 is used to represent the net loss of solids from the dense bed surface into the transport zone. The following chapter introduces modifications to this expression to account for polydisperse solids mixtures to represent size-dependent entrainment fluxes.

2.2.2.2 Transport Zone

Inside the freeboard, the macroscopic solids flow forms a core-annulus pattern. In the core region, a fraction of the solids is transported downward due to differences in particle size or density, leading to disengagement from the upward gas flow, while the remaining solids are carried upward. Simultaneously, upward-moving solids are continuously dispersed laterally into the annulus region, with downwards-flowing wall layers that contribute to the solids back-mixing into the dense bed [28]. A fraction of the solids that reach the top of the furnace is back-mixed into the wall layers, quantified by the solids separation efficiency, η_{ss} [29]. The remaining particles leave the furnace and enter the cyclone. Figure 2.4 shows a simplified representation of the flow patterns that are present in the upper part of the freeboard.

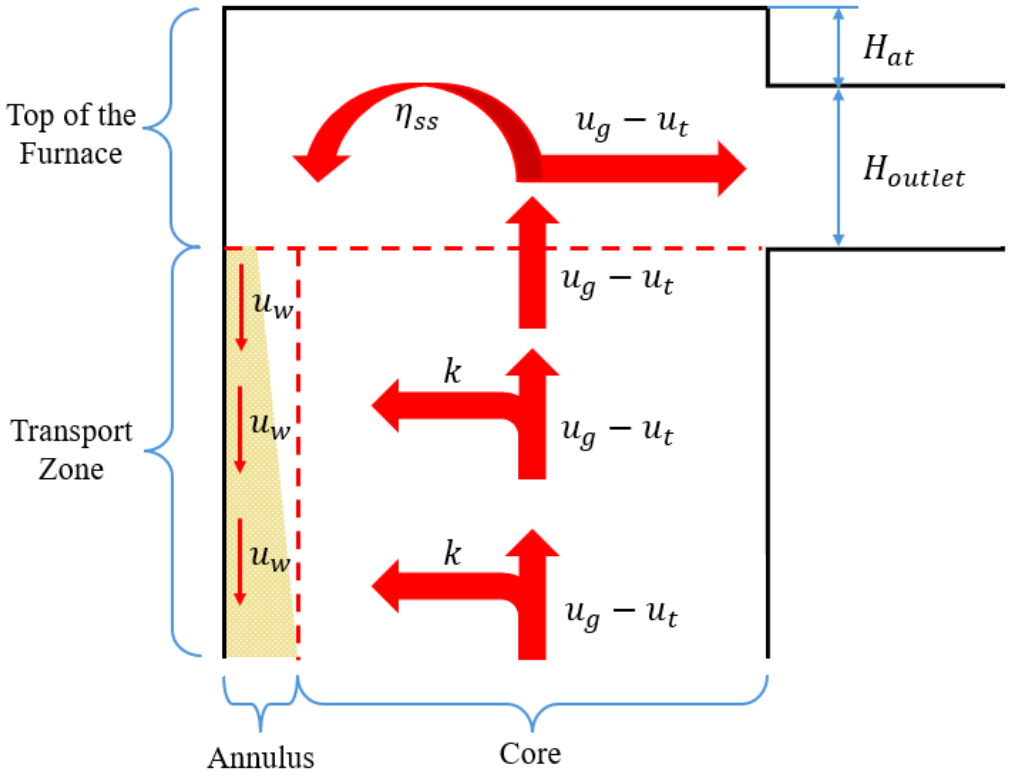

Figure 2.4: Simplified representation of the flow patterns in the upper freeboard.

2.2.2.2.1 Core-Annulus Pattern As discussed by Wu et al. [28], the coexistence of upward and downward flows in the core region results in a net upward flow. For this reason, the core region in this work is modeled as a unidirectional upward flow, with particles moving at their slip velocity (defined as the difference between the gas and particle terminal velocity) [7]. The resulting solids mass flow in the core of the transport zone, $\dot{m}_{core,fb}$, is expressed as:

$$\dot{m}_{core,fb} = C_{s,core} A_{core} (u_g - u_t) \tag{2.13}$$

where $C_{s,core}$ is the solids concentration at the core and A_{core} is the cross-sectional area of flow. Equation 2.13 assumes that the terminal velocity remains constant along the furnace height, neglecting the effect of size segregation, which can alter the effective terminal velocity [3].

For the annulus region, a constant downward wall velocity, u_w, is assumed. The corresponding wall layer mass flow, $\dot{m}_{ann,fb}$, is formulated similarly to the core as:

$$\dot{m}_{ann,fb} = C_{s,ann} A \cdot u_w \tag{2.14}$$

where $C_{s,ann}$ is the solids concentration in the annulus and A_{ann} is the cross-sectional area of flow. This flow area increases downstream due to changes in the wall layer thickness, t_{wall}, as shown in Figure 2.4. The thickness increases as it gets closer to the dense bed, depending only on height once circulation conditions are established. Pallarès et al. [7] described the change of t_{wall} as a height-dependent function: for heights above a saturation height, H_{sat}, the annulus thickness decreases linearly with height. Below the saturation height, the flow is considered to be part of the splash zone, where the solids flow pattern is different, and the thickness of the wall layer is assumed constant. Thus, the wall layer thickness is modeled as:

$$t_{wall}(h) = 0.0108(H_0 - h), \text{for } H_{sat} < h \leq H_{duct} \tag{2.15}$$

$$t_{wall} = 0.0648 \varnothing_h, \text{for } h \leq H_{sat} \tag{2.16}$$

where H_{outlet} is the cyclone duct height, H_0 is the height of the furnace, and $\varnothing_h$ is the equivalent (hydraulic) diameter, defined as $4A/P$, and with H_{sat} defined as:

$$H_{sat} = H_0 - 6\varnothing_h \tag{2.17}$$

In large-scale CFB units, aspect ratios are typically lower than 10. Equation 2.17 takes an AR of 6 to estimate H_{sat}, as the transition to the splash zone is found at heights with local ARs exceeding this value. Accurate representation of the wall-layer thickness is fundamental, as it has a considerable impact on heat transfer modeling [7].

2.2.2.2.2 Lateral Transport of Solids As discussed before, solids transported upward in the transport zone continuously migrate to the wall layers. In the present work, the lateral mass transfer of solids, $\dot{m}_{lat}$, is expressed as:

$$\dot{m}_{lat} = k \cdot C_s A_{lat} \tag{2.18}$$

Djerf et al. [30] proposed a model for the lateral transport of solids based on simulations and experimental data for large-scale CFB units, where the mass transfer coefficient, k, is given by:

$$k = 0.029 \cdot (u_g - u_t)^{1.05} \cdot \varnothing_h^{0.72} \tag{2.19}$$

This correlation considers typical gas properties for large-scale CFB combustion, with $\rho_g = 0.33$ kg/m^3 and $\mu_g = 4.3 \times 10^{-5}$ Pa $\cdot$ s, neglecting vertical dispersion of solids to simplify the analysis. The mass transfer coefficient calculated by Equation 2.19 represents the net lateral solids transport, implicitly including both transport directions, with the dominant solids transport contribution occurring from the core to the annulus. For the representative systems analyzed by Djerf et al. [30], k typically takes values between 0.01 and 1 m/s. The dependence of Equation 2.19 on the slip velocity also suggests that secondary air injection, by increasing gas velocity above the injection height, may increase the lateral mass transport, enhancing solids transfer from the upward core flow to the downward annulus flow.

2.2.2.2.3 Solids Separation Efficiency As indicated by Figure 2.4, not all particles exit the riser to the cyclone. The fraction of solids that remains in the furnace contributes to the descending wall layers [29]. The solids separation efficiency, η_{ss}, quantifies this behavior by relating the solids flow being back-mixed to the annulus to the incoming solids flow into the top of the furnace:

$$\eta_{ss} = \frac{\text{Solids back-mixed to the wall layers}}{\text{Solids reaching the top of the furnace}} \tag{2.20}$$

Thus, the lateral mass transfer of solids back-mixed to the annulus at the top of the furnace, $\dot{m}_{lat,top}$, is defined as:

$$\dot{m}_{lat} = \eta_{ss} \cdot \dot{m}_{core,fb} \tag{2.21}$$

Wu et al. [29] analyzed the influence of outlet geometry and gas velocity through CFD simulations. The resulting correlation for the solids separation efficiency is given by:

$$\eta_{ss} = 1 - f_0 f_1 \left(\frac{S_{\text{outlet}}}{S_0}\right) f_2 \left(\frac{H_{\text{outlet}}}{W_{\text{outlet}}}\right) f_3 \left(\frac{H_{\text{at}}}{D}\right) \tag{2.22}$$

where S_{outlet} is the cross-sectional area of the outlet duct, S_0 is the cross-sectional area of the riser, H_{outlet} and W_{outlet} are the height and width of the outlet duct, respectively, H_{at} is the distance between the roof of the riser and the top of the outlet duct, and D is the characteristic length, taken as the normal distance from the outlet duct to the riser wall (equivalent to the riser depth, D_0) [29].

The f-terms are expressed as functions of the Stokes number, St, defined as:

$$St = \frac{d_p^2 u_g \rho_s}{18 \mu_g D} \tag{2.23}$$

The individual terms are given by:

$$f_0 = 0.99 - 0.09 \ln(200 \cdot St) \tag{2.24}$$

$$f_1 \left(\frac{S_{\text{outlet}}}{S_0} \right) = 1 - (0.16 \ln St + 0.6) \left(1 - \frac{S_{\text{outlet}}}{S_0} \right) \tag{2.25}$$

$$f_2 \left(\frac{H_{\text{outlet}}}{W_{\text{outlet}}} \right) = 1 \tag{2.26}$$

$$f_3 \left(\frac{H_{\text{at}}}{D} \right) = 1 - 0.085 \left(\frac{H_{\text{at}}}{D} \right) \tag{2.27}$$

Together, these expressions describe the solids separation efficiency as a function of particle characteristics, gas properties, and boiler geometry. The combined expression (Equation 2.22) is valid for St ≥ 0.035. It is assumed in this work that particles that have a Stokes number smaller than this are carried by the gas directly to the cyclone, and their separation efficiency is 0. Furthermore, it is assumed for simplicity that the solids mass flow leaving the furnace to the cyclone has the same definition as the transport zone core region flow, given by Equation 2.13.

Wu et al. [29] derived this correlation for a boiler with a single cyclone. In the present work, to account for multiple cyclones, the ratio of cross-sectional areas in Equation 2.25 is multiplied by the number of cyclones. This is equivalent to dividing the riser's cross-sectional area into equal parts per cyclone.

2.3 Biomass Conversion Modeling

In the presence of a hot gas stream, solid fuel particles undergo three mechanisms of mass loss: drying, devolatilisation, and char combustion [31]. These conversion stages are strongly influenced by the physical properties of the fuel, as well as by external conditions like temperature and heating rate [32]. In this section, the biomass composition characteristics are described, followed by the key considerations and assumptions adopted for the modeling of the conversion stages for biomass combustion.

2.3.1 Biomass Composition

The knowledge of the biomass composition is highly relevant for modeling its thermochemical conversion. As a high-volatile fuel, biomass typically exhibits a high content of volatiles, between 65 and 85% on a mass basis [33]. Fixed carbon content (the responsible for char formation) and moisture make up most of the remaining mass fraction, each ranging between 10 and 30% [34] depending on the fuel source

and prior treatments. Based on additional data reported by Kumar et al. [32], Table 2.1 summarizes the typical composition for Swedish wood. The ash content can usually be neglected, as it represents a minor fraction of the total mass (approximately 0.1%).

Property	Composition (wt%)
Moisture	10
Volatiles	78
Fixed Carbon	12

Table 2.1: Biomass composition from Swedish wood

2.3.2 Conversion Stages

Upon injection into the furnace, heat is convected and radiated to the biomass particles' surface, and is then conducted inwards. The water present in the fuel (indicated by the moisture content) evaporates and flows outwards through each of the particles' pores [31]. Once the drying is completed, the temperature rises, and the biomass particles decompose, releasing volatiles. For large fuel particles, such as woodchips, the temperature distribution is uneven across the particle, leading to localized conversion as the rates of drying and devolatilisation depend on temperature [31]. After the volatiles are released, highly porous char remains. Oxygen in the surrounding gas flows through the pores and starts the combustion process until the remaining char converts into combustion gases like CO and CO_2. This process lasts much longer than the devolatilisation and drying stages [31].

In the present work, the conversion stages are modeled as first-order global reactions to describe mass loss [31], based on characteristic times for conversion. As stated by Gomez-Barea et al. [34], this approach is sufficient for initial estimates of the biomass conversion. Fuel properties, taken from Table 2.1, are assumed to remain constant during all conversion stages. The wet biomass woodchips enter the furnace at a constant feeding rate, $\dot{m}_{fuel,in}$, and undergo drying. The mass balance for the wet biomass is expressed as:

$$V\frac{dC_{wet}}{dt} = \dot{m}_{fuel,in} - C_{wet}V\frac{1}{\tau_1} \tag{2.28}$$

where τ_1 is the characteristic drying time. As moisture is removed, the biomass begins the devolatilisation stage. The mass balance for the dry biomass is then defined as:

$$V\frac{dC_{dry}}{dt} = (1 - X_{\text{moist}})C_{wet}V\frac{1}{\tau_1} - C_{dry}V\frac{1}{\tau_2} \tag{2.29}$$

where τ_2 is the characteristic devolatilisation time. During drying, part of the biomass mass is removed as water vapor, which mixes with the gases in the furnace.

A similar mathematical description applies to char formation and conversion:

$$V\frac{dC_{char}}{dt} = \left(\frac{X_{\text{char}}}{X_{\text{char}} + X_{\text{vol}}}\right) C_{dry} V \frac{1}{\tau_2} - C_{char} V \frac{1}{\tau_3} \tag{2.30}$$

where τ_3 is the characteristic char conversion time. Since biomass contains a high fraction of volatiles, only a limited fraction of the dry fuel mass remains as char after devolatilisation. Most of the mass is removed into the circulating gas phase as volatiles.

The characteristic conversion times, τ, can be estimated analytically or experimentally. The compendium on solid fuel conversion by Thunman [31] presents both empirical correlations and analytical formulations for the characteristic times for each stage. Such expressions are included in Appendix A for reference. Additionally, Gomez-Barea et al. [34] performed empirical characterizations for the total time to release 90% of the volatiles content from biomass pellets, with an as-received composition of 6.28% moisture and 75.89% volatiles. At a bed temperature of 850°C, the combined drying and devolatilisation time was approximately 55 s.

In the present work, the characteristic times summarized in Table 3.9 are selected based on a combination of analytical estimates and empirical observations for similar fluidization applications. These values are intended to provide representative conversion time scales rather than exact kinetic predictions.

Conversion Stage	Characteristic Time [s]
Drying, τ_1	20
Devolatilisation, τ_2	40
Char Combustion, τ_3	200

Table 2.2: Characteristic times for conversion stages

2.3.3 Size and Density Changes during Conversion

During conversion, biomass particles can undergo volumetric shrinkage and fragmentation [32]. Combined with the loss of solid mass through moisture evaporation and volatile release, these processes lead to variations in particle size and density, directly influencing conversion time and particle hydrodynamics. However, accurate modeling of these phenomena can be highly complex, as many factors and properties need to be considered [32]. In the present work, the size and density changes are treated using a simplified stage-wise approach. The particle properties are assumed to change instantaneously at the transition between stages and to remain constant within each stage. The selected shrinkage rates are based on experimental results found in the literature.

Rezaei et al.[35] proposed empirical correlations relating particle-size shrinkage during drying to the initial moisture content. For the reference biomass composition given in Table 2.1, the particle diameter after drying decreases by approximately

7% relative to the as-received value. Furthermore, Kumar et al.[32] reported a volumetric shrinkage after devolatilisation ranging between 35.6 and 58.4% of the initial biomass volume. In the present work, a fixed volumetric shrinkage of 42% is adopted for the devolatilisation stage. To account for fragmentation following devolatilisation, an additional particle size reduction of 75% is assumed for char particles. The fragmentation process is assumed to only affect particle size and does not have an effect on the final char density. Table 2.3 shows the principal physical properties of biomass during each stage. Despite losing 10% of the initial particle mass during drying, the diameter shrinkage of 7% corresponds to a volumetric shrinkage close to 20%, causing the particle density of the dry fuel particles to increase. Additionally, all biomass particle classes are assigned a sphericity, ϕ, of 0.2.

State of the Particles	Total Size Reduction [%]	d_p [mm]	ρ_s [kg/m^3]
As-Received	–	20	500
Dried	7	18.6	559.45
Devolatilized (Char)	85.5	2.9	307.52

Table 2.3: Characteristic particle properties for each conversion stage. Detailed explanation of the calculation of densities and sizes is provided in Appendix B.

3
Method

3.1 Model Overview

In the present work, a transient 1.5D semi-empirical model is developed to describe the solids hydrodynamics and fuel conversion inside an industrial CFB boiler. While the model is developed with a particular focus on biomass-fired boilers, the formulation aims to remain sufficiently general to be applicable to a wide range of CFB systems.

The furnace is discretized vertically to account for the different fluid-dynamic regions described in Chapter 2 and divided radially into core and annulus regions. As illustrated by Figure 3.1, the model receives as inputs the geometrical and operational characteristics of the boiler, together with the physical properties of the gas and solid phases. The governing transient mass balances are formulated as a coupled system of ordinary differential equations (ODEs), solved using the SciPy library in Python. The solution of the ODE system provides the temporal and spatial evolution of the solids concentrations, mass flows, and fuel conversion in the furnace.

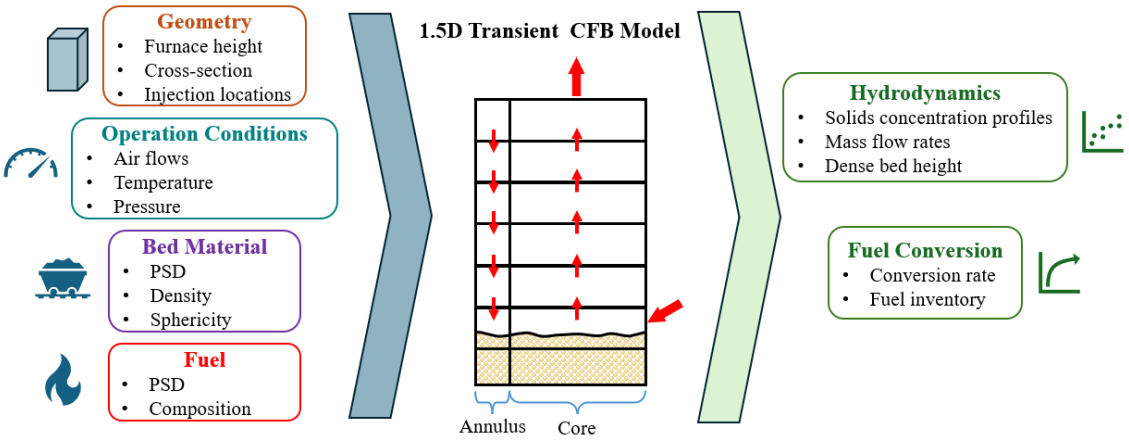

Figure 3.1: Model schematic showing inputs and outputs

3.2 Computational Mesh

The computational mesh spans the entire furnace region. The cyclone and loop seal are not represented explicitly; instead, they are modeled as outgoing and incoming

flow terms, respectively. The subdivision of the computational domain into different fluid-dynamical regions is fundamental to the model formulation, since each zone has a particular mathematical description. In the present work, the splash zone is not represented as a separate physical region. Instead, its effect is accounted for through an entrainment flow that transfers particles to the freeboard directly from the dense bed (see Equation 2.11).

The position of the dense bed varies with time, causing the vertical layers associated with the dense bed and freeboard regions to change dynamically during the simulation. Thus, the extent/height of the dense bed must be continuously tracked to identify which computational cells belong to the dense bed region and which belong to the freeboard. Since this operation is performed at every solver step, computational efficiency needs consideration. To improve computational efficiency, Boolean indexing is used to assign the vertical layers to their corresponding fluid-dynamical regions. This vectorized approach simplifies the formulation of the governing equations and reduces computational cost. Figure 3.2 illustrates the computational mesh and the indices assigned to the relevant vertical layers used in the model formulation. Table 3.1 describes the layer indices. The red indices shown on the right-hand side of the diagram denote subsets of the computational layers requiring specific mathematical treatment in the governing equations, such as the application of source terms or region-specific formulations. A detailed description of the logical statements used in their definition can be found in Appendix C.

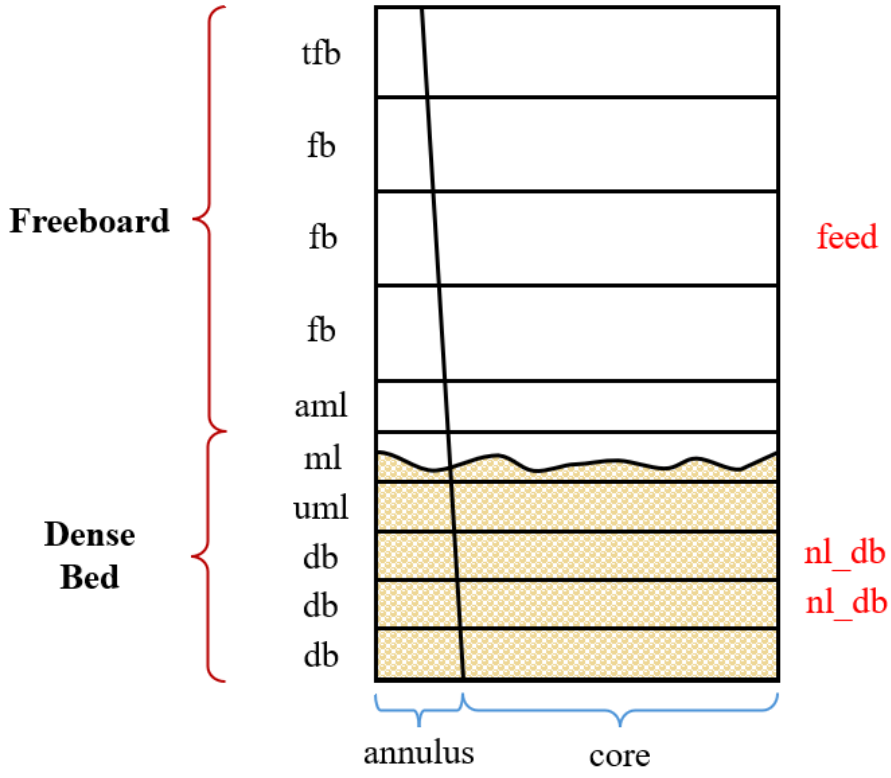

Figure 3.2: Computational mesh layout with indexing.

Index	Meaning	Description
tfb	Top-of-the-Freeboard	Topmost layer of the domain, corresponding to the top of the furnace.
fb	Freeboard	Freeboard layers excluding the top of the furnace and the layer above the dense bed.
feed	Solids recirculation inlet	Position in the Freeboard where solids are recirculated into the furnace from the feedback loop.
aml	Above Mixed Layer	Layer directly above the dense bed top. It is part of the Freeboard.
ml	Mixed Layer	Layer where the top of the dense bed is currently located.
uml	Under Mixed Layer	Layer directly below the top of the dense bed.
db	Dense Bed	Dense bed layers.
nl_db	Dense Bed excluding bottom layer	Layers in the dense bed excluding the bottom boundary layer.

Table 3.1: Vertical indexing of the computational domain.

To provide higher spatial resolution in the dense bed region, where solids mixing is most significant, while accounting for the annulus width variation along the furnace height, a non-uniform computational mesh is adopted. Fine cells are concentrated in the lower furnace region, while coarser cells are primarily used in the freeboard. The mesh is constructed using two different cell heights, determined from the system dimensions, the desired number of fine and coarse layers (n_{fine} and n_{coarse}, respectively), and the layer height ratio, R_h, defined as:

$$R_h = \frac{h_{\text{coarse}}}{h_{\text{fine}}} \tag{3.1}$$

The influence of the number of layers and the height ratio is investigated in Section 3.5. Details regarding the calculation of cell heights, areas, and volumes are provided in Appendix C.

3.3 Governing Equations and Model Formulation

3.3.1 Conservation Equations

The solids species mass balance is formulated as the combined effect of hydrodynamic transport and fuel conversion processes. For each computational cell, the transient balance for a given solids species is expressed as:

$$V_{\text{cell}} \frac{dC_s}{dt} = \dot{m}_{\text{net}} + S_{\text{f}} + S_{\text{c}} \tag{3.2}$$

where C_s is the solids concentration, V_{cell} is the cell volume, $\dot{m}_{\text{net}}$ is the net mass transport in the cell, and S_{f} and S_{c} represent the feeding and conversion source terms, respectively.

The net transport term includes both diffusive and convective contributions through the top, bottom (bot), and lateral (lat) cell faces:

$$\dot{m}_{\text{net}} = [J_{\text{top}} + J_{\text{bot}} + J_{\text{lat}}]_{\text{cell}} + [D_{\text{top}} + D_{\text{bot}} + D_{\text{lat}}]_{\text{cell}} \tag{3.3}$$

with J and D denote convective and diffusive mass transport terms, respectively. The sign convention of each face flux determines the direction of the mass transfer. In turn, the formulation of the transport terms depends on the fluid-dynamic region represented by the computational cell.

3.3.2 Solids Hydrodynamics Modeling

3.3.2.1 Dense Bed Layers Formulation

The dense bed formulation aims to represent the dynamic evolution of the bed while preserving the solids mixing behavior described in Chapter 2. To identify the computational layers belonging to the dense bed at a given instant, a local solids fraction criterion is used:

$$\varepsilon_s + \delta > \varepsilon_{\text{layer}} > \varepsilon_s - \delta \tag{3.4}$$

where δ is the comparison threshold used to determine whether a layer belongs to the dense bed region. Layers up to **uml** are considered fully occupied by bed material and therefore satisfy Equation 3.4. The **ml** layer is defined as a mixed layer, since it may only be partially occupied by bed material, resulting in a lower local solids fraction than the underlying layers. Due to the dynamic behavior of the bed, the solids fraction in layer **ml** can increase or decrease. When the solids fraction in the layer reaches the maximum packing limit, the layer becomes fully incorporated into the dense bed, and the mixed layer shifts upward by one computational layer. Similarly, when the solids fraction in layer **ml** decreases until approaching that of layer **aml**, the mixed layer shifts downward. The position of the dense bed is therefore determined by the evolution of the mixed layer.

Once the dense bed region has been identified, the corresponding transport equations can be formulated. In accordance with the definitions and assumptions described in Chapter 2, transport within the dense bed is represented primarily through diffusive mechanisms, with limited convective transport contributions, as illustrated in Figure 3.3.

The hydrodynamic mass balance for the core and annulus regions of all dense bed layers identified with index **db** is expressed as:

$$V_{\text{cell}} \frac{dC_s}{dt} = D_{\text{top}} + D_{\text{bot}} + D_{\text{lat}} \tag{3.5}$$

with the exception of the layer at the bottom of the furnace, having:

$$D_{\text{bot}} = 0$$

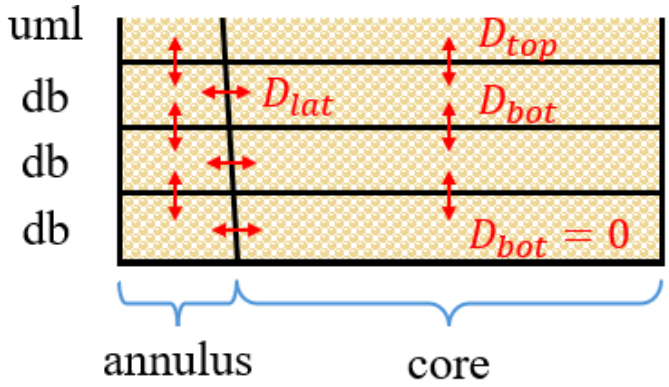

Figure 3.3: Diffusive transport flows in the lower dense bed layers. Red arrows indicate possible transport paths.

As described in Equation 2.9, the diffusive mass exchange within the dense bed is represented through the dispersion coefficients and the concentration gradients between neighboring cells. While the core-annulus structure is less relevant in the dense bed region, the radial subdivision is retained in the computational domain for consistency with the remaining model formulation. Thus, in the lateral direction, the diffusive mass exchanges are defined as:

$$D_{\text{lat,core}} = D_h A_{\text{lat}} (C_{\text{s,annulus}} - C_{\text{s,core}}) \tag{3.6}$$

$$D_{\text{lat,annulus}} = D_h A_{\text{lat}} (C_{\text{s,core}} - C_{\text{s,annulus}}) \tag{3.7}$$

where the concentration gradients determine the direction of the mass transport. The transport term is defined as positive when solids enter a given cell, indicating higher neighboring concentrations than the local cell concentration. As mentioned in Chapter 2, a sufficiently large dispersion coefficient is chosen to promote nearly instantaneous mixing of solids in the lateral direction, maintaining approximately uniform solids concentration within each layer. Consequently, the characteristic transport length Δx from Equation 2.9 is neglected in the formulation.
A similar formulation is applied for the vertical diffusive transport:

$$D_{\text{top}} = \frac{D_v}{\Delta z} A_{\text{top}} (C_{\text{s,upper}} - C_{\text{s,db}}) \tag{3.8}$$

$$D_{\text{bot}} = \frac{D_v}{\Delta z} A_{\text{bot}} (C_{\text{s,lower}} - C_{\text{s,db}}) \tag{3.9}$$

with the characteristic transport distance, Δz, defined as the distance between the centers of neighboring computational cells. Unlike the lateral transport, the vertical transport length is retained since the vertical solids exchange is not assumed to

happen instantaneously.

For the upper dense bed region (indices **uml** and **ml**), additional convective transport terms are introduced, as illustrated in Figure 3.4. The hydrodynamic mass balance is then expressed as:

$$V_{\text{cell}} \frac{dC_s}{dt} = D_{\text{top}} + D_{\text{bot}} + D_{\text{lat}} + J_{\text{top}} + J_{\text{bot}} + J_{\text{lat}} \tag{3.10}$$

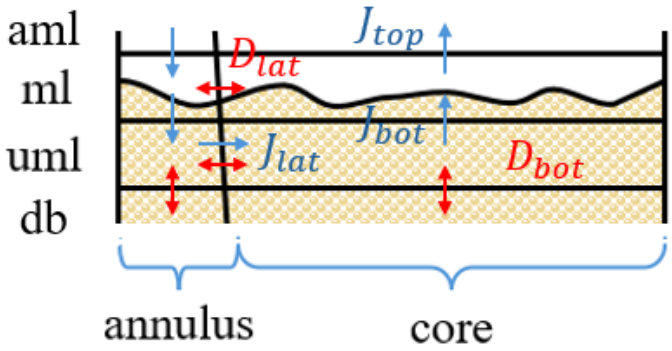

Figure 3.4: Transport flows in the upper dense bed region. Blue and red arrows represent the convective and diffusive terms, respectively.

In layer **uml**, the upper-face diffusive transport terms are replaced by unidirectional convective flows. These additional transport terms are introduced to maintain communication between the dense bed and the tracking layers, and to preserve solids mixing near the dense-bed surface. Solids returning from the freeboard annulus induce a net flow of solids into the upper dense bed region. The resulting concentration differences are redistributed through lateral and vertical convection between the annulus, core, and layers. This recirculation loop enables solids entrained into the freeboard to be replenished within the bed.

The convective transport terms are particularly important for polydisperse solids systems, where each size class can experience substantially different entrainment rates. Smaller and lighter particles tend to be entrained faster than larger particles. Without the convection loop, diffusion alone may lead to unrealistic depletion of specific size or density classes from the dense bed without a corresponding evolution of the dense bed height. Thus, the introduced convective terms provide a mechanism for consistent solids mixing at the upper dense bed.

The convective transport terms are defined from the volumetric flow of solids, $\dot{V}$, entering the mixed layer of the dense bed from the freeboard annulus, moving at constant wall velocity as defined in Equation 2.14. The total volumetric flow accounts for all solids classes being recirculated into the dense bed:

$$J_{\text{top,ml,annulus}} = C_{s,\text{aml,annulus}} A_{\text{bot,aml,annulus}} u_w \tag{3.11}$$

$$\dot{V} = \sum_{i=1}^{\text{solids}} \frac{(J_{\text{top,ml,annulus}})_i}{\rho_{s,i}} \tag{3.12}$$

For each solids class, the convective loop terms are weighted according to their local contribution to the total solids fraction within the corresponding computational cell. The convective terms for each solids class i are expressed as:

$$J_{\text{top,uml,core},i} = -J_{\text{bot,ml,core},i} = -\dot{V}\rho_{s,i} \cdot \left(\frac{\varepsilon_{s,i}}{\varepsilon_s}\right)_{\text{uml,core}} \tag{3.13}$$

$$J_{\text{top,uml,annulus},i} = -J_{\text{bot,ml,annulus},i} = \dot{V}\rho_{s,i} \cdot \left(\frac{\varepsilon_{s,i}}{\varepsilon_s}\right)_{\text{ml,annulus}} \tag{3.14}$$

$$J_{\text{lat,uml,core},i} = -J_{\text{lat,uml,annulus},i} = \dot{V}\rho_{s,i} \cdot \left(\frac{\varepsilon_{s,i}}{\varepsilon_s}\right)_{\text{uml,annulus}} \tag{3.15}$$

$$J_{\text{lat,ml},i} = J_{\text{bot,uml},i} = 0$$

Furthermore, the upper-face convective flow in the core region of layer **ml** corresponds to the solids entrainment flow defined in Equation 2.12. Following the treatment applied to the convective loop terms to avoid unrealistic depletion of specific solid classes, the entrainment mass flow expression is conditioned by the local contribution of each solids class to the total solids fraction. Thus, when the concentration of a solids class approaches zero, so does its associated entrainment rate:

$$J_{\text{top,ml,core},i} = -\rho_{s,i} \cdot \left(u_{g,\text{top}} A_{\text{top}} G^*_{s,e,i} \frac{\varepsilon_{s,i}}{\varepsilon_s}\right)_{\text{ml,core}} \tag{3.16}$$

The lateral diffusive terms, D_{lat}, in the **uml** and **ml** layers employ the definition given in Equation 3.6 and Equation 3.7. The bottom diffusive terms in layer **uml** keep the formulation defined in Equation 3.9. The remaining diffusive terms are not present for these layers, thus:

$$D_{\text{bot,ml}} = D_{\text{top,ml}} = D_{\text{top,uml}} = 0$$

An important consideration must be made for fuel particles undergoing conversion. During combustion, char particles sublimate and incorporate into the gas phase, reducing their contribution to the solids fraction. Directly incorporating this reduction into the dense-bed tracking procedure may lead to artificial changes in the identified bed position. Since fuel conversion causes progressive loss of solids inventory, fuel particles are excluded from the dense bed tracking criteria. Thus, the evolution of the dense bed depends solely on the bed-material hydrodynamics. Fuel particles still follow the same hydrodynamic formulations defined in this and the upcoming sections, while inheriting the dynamic indexing from the bed-material-based dense bed tracking.

The formulation of the convective loop terms is modified for fuel particles. Since these particles do not contribute to the dense-bed tracking procedure, the solids-fraction balancing mechanism is no longer required, and the lateral convective term in layer **uml**, J_{lat}, is removed, as indicated in Figure 3.5. Furthermore, the upper-face convective terms in layer **uml**, J_{top}, together with the corresponding lower-face

terms in layer **ml**, J_{bot}, are modified to preserve the incoming and outgoing flows between the dense bed and the freeboard at the upper faces of the **ml** layer.

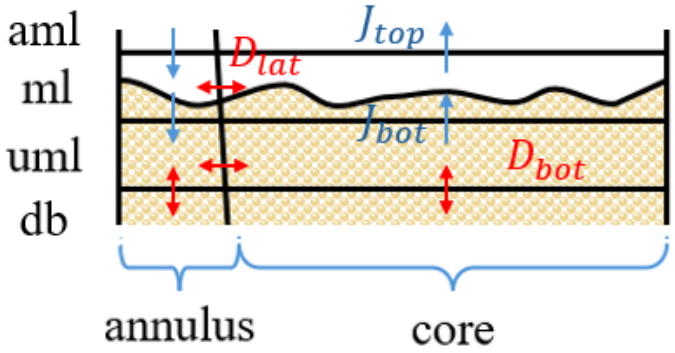

Figure 3.5: Transport flows in the upper dense bed region for fuel particles. The term J_{lat} is absent in this formulation.

$$J_{\text{top,uml,core},i} = -J_{\text{bot,ml,core},i} = -\rho_{s,i} \cdot \left(A_{\text{top}} \frac{\varepsilon_{s,i}}{\varepsilon_s}\right)_{\text{uml,core}} \left(u_{g,\text{top}} G^*_{s,e,i}\right)_{\text{ml,core}} \tag{3.17}$$

$$J_{\text{top,uml,annulus},i} = -J_{\text{bot,ml,annulus},i} = C_{s,\text{ml,annulus}} A_{\text{bot,ml,annulus}} u_w \tag{3.18}$$

3.3.2.2 Freeboard Layers Formulation

The freeboard mass balance formulation is governed by convective transport terms. The formulation remains largely uniform, with specific treatments applied to the **aml** and **tfb** layers. The mass balance for the freeboard can be expressed as:

$$V_{\text{cell}} \frac{dC_s}{dt} = J_{\text{top}} + J_{\text{bot}} + J_{\text{lat}} \tag{3.19}$$

A schematic representation of the transport mechanisms in the lower freeboard region is shown in Figure 3.6.

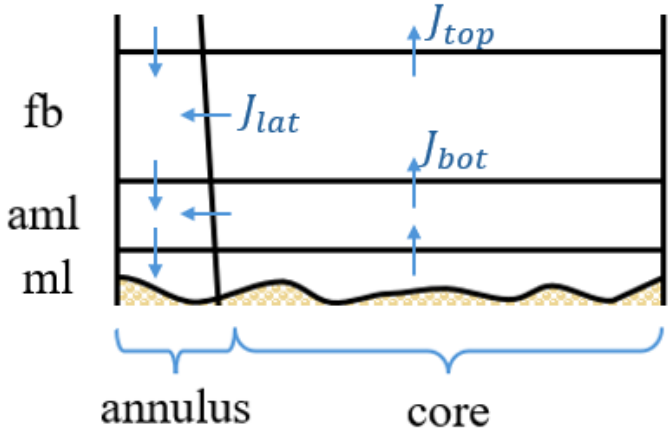

Figure 3.6: Transport flows in lower freeboard region.

Upward transport in the core region is represented by the slip velocity, while downward transport in the annulus region is given by a constant wall velocity. The lateral mass transfer coefficient, k, controls the solids transfer from core to annulus. The sign convention follows the definition introduced previously, where positive values denote transport into the computational cell. The convective transport terms in the mass balance for each solids class can then be expressed as:

$$J_{\text{top,fb,core}} = -C_{s,\text{fb,core}}(u_{g,\text{top}} - u_t)A_{\text{top,fb,core}} \tag{3.20}$$

$$J_{\text{top,fb,annulus}} = C_{s,\text{upper,annulus}}u_w A_{\text{top,fb,annulus}} \tag{3.21}$$

$$J_{\text{bot,fb,core}} = C_{s,\text{lower,core}}(u_{g,\text{bot}} - u_t)A_{\text{bot,fb,core}} \tag{3.22}$$

$$J_{\text{bot,fb,annulus}} = -C_{s,\text{fb,annulus}}u_w A_{\text{bot,fb,annulus}} \tag{3.23}$$

$$J_{\text{lat,fb,core}} = -J_{\text{lat,fb,annulus}} = -kC_{s,\text{fb,core}}A_{\text{lat,fb,core}} \tag{3.24}$$

Layer **aml** requires special treatment because it represents the transition between the dense bed and freeboard regions. Thus, the lower-face transport term is replaced by the solids entrainment flow originating from layer **ml**:

$$J_{\text{bot,aml,core},i} = \rho_{s,i} \cdot \left(u_{g,\text{top}}A_{\text{top}}G^*_{s,e,i}\frac{\varepsilon_{s,i}}{\varepsilon_s}\right)_{\text{ml,core}} \tag{3.25}$$

A schematic representation of the upper freeboard is shown in Figure 3.7.

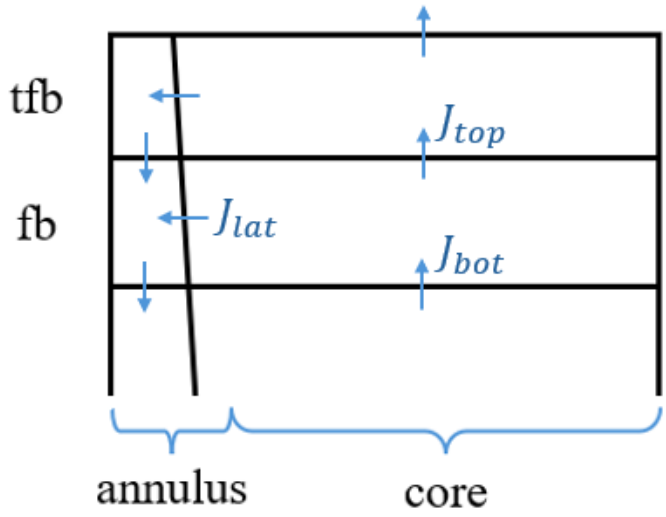

Figure 3.7: Transport flows in upper freeboard region.

The mass balance defined by Equation 3.19 also applies for the **tfb** layer. However, the convective transport terms require special treatment due to their location at the top of the computational domain. The annulus region has no upper-face transport term, J_{top}, as this is the first annulus cell of the mesh. The only incoming transport to the annulus region is the lateral transfer from the core, defined through the solids separation efficiency, η_{ss}, as described in Chapter 2. The modified transport terms for this layer are described ass:

$$J_{\text{top,tfb,annulus}} = 0$$

$$J_{\text{lat,tfb,core}} = -J_{\text{lat,tfb,annulus}} = -\eta_{ss} C_{s,\text{fb,core}} (u_{g,\text{bot}} - u_t) A_{\text{bot,tfb,core}} \tag{3.26}$$

3.3.2.3 Cyclone–Loop Seal Feedback Formulation

In the present work, the representation of the cyclone and loop seal is simplified as outgoing and incoming flows, respectively. Figure 3.7 includes an arrow in the upper face of the core region in layer **tfb**. This convective term, J_{top}, represents the solids flow entering the cyclone and is defined as indicated in Equation 3.20. Furthermore, the cyclone is assumed to operate with a separation efficiency of 1, implying complete solids capture. Thus, only gas exits the system, resulting in a closed solids inventory.

The returning solids flow from the loop seal is introduced into the annulus region of the freeboard at layer **feed**. This allows the solids to return to the dense bed through the downward flow of the annulus. The recirculated solids are incorporated into the mass balance through a feeding source term, such that:

$$S_{\text{f,feed,annulus}} = J_{\text{top,tfb,core}} \tag{3.27}$$

This treatment preserves mass conservation between the outgoing cyclone flow and the returning solids stream. No residence time or solids accumulation is considered in the external circulation loop.

3.3.2.4 Gas Velocity Considerations

In the present model, the primary air establishes the initial superficial gas velocity at the furnace inlet. Additional contributions from secondary air are introduced at prescribed heights in the furnace, producing local increases in gas velocity above the injection points. The gas velocity at a given vertical position can then be expressed as:

$$u_g(h) = u_{g,\text{PA}} + u_{g,\text{SA}}(h) \tag{3.28}$$

where $u_{g,\text{PA}}$ and $u_{g,\text{SA}}$ represent the primary and secondary air velocity contributions, respectively. In the absence of secondary air injection, the gas velocity remains constant along the furnace height, since changes in gas flow due to fuel conversion and gas-phase species evolution are neglected in the present work.

3.3.3 Reactions Modeling

Fuel conversion is represented through source terms added to the solids mass balance. Conversion is assumed to start as soon as the fuel enters the furnace, and the conversion processes can take place in any spatial region of the furnace. For simplicity, the fuel is injected in layer **aml**, allowing the fuel particles to reach the dense bed rapidly and undergo solids mixing. As described in Chapter 2, fuel particles undergo drying, devolatilisation, and char combustion, with continuous mass transfer

between conversion states according to the fuel composition and characteristic conversion times. The drying, devolatilization, and char combustion source terms are defined over the whole furnace by Equation 2.28, Equation 2.29, and Equation 2.30, respectively.

Fuel injection is given as a feeding source term in layer **aml** at a constant inlet mass flow. Numerical activation of this feeding term is discussed in Section 3.4:

$$S_{\text{f,aml,annulus}} = \dot{m}_{fuel,in} \tag{3.29}$$

3.4 Model Architecture and Numerical Implementation

3.4.1 Computational Framework

The model described in the previous sections was implemented in Python using a modular computational framework. The implementation was structured to separate the different physical and numerical components of the model, including system geometry, hydrodynamics and fuel conversion calculations, numerical integration, and post-processing routines. Input parameters related to operating conditions, reactor geometry, and solids properties were organized using Python DataClasses to facilitate parameter management and improve model readability.

The modular structure enabled the hydrodynamics and fuel conversion formulations to be evaluated independently during model development and verification. In addition, input loading, calculation routines, and post-processing procedures were organized into separate scripts to improve maintainability and facilitate future model extensions. A detailed overview of the script organization is provided in Appendix D.

3.4.2 Data Structure

The dependence of the model variables on spatial regions and solids properties requires a multidimensional data structure, capable of storing and retrieving model information for any location within the discrete space and for any solids category. For this purpose, the principal state variables and model parameters were organized in a five-dimensional structure consisting of two spatial dimensions and three solids-properties dimensions:

(layer, region, family, size, state)

Within this structure, the first two dimensions locate the model information spatially, where **layer** corresponds to the vertical position and **region** identifies either the core or annulus regions. The remaining dimensions describe the solids characteristics, specifically the solids family, particle size, and conversion state. Thus,

each element within the data structure represents a specific solids category at a defined spatial location within the furnace. Furthermore, together with the indexing approach described in Section 3.2, the organizational structure facilitates the numerical implementation of the model, allowing operations to be performed simultaneously across selected dimensions while preserving spatial and physical consistency.

The extent of each dimension is not fixed and depends on the system's modeling requirements. Particularly, the number of particle families depends on the solids present in the system; the number of size classes depends on the desired particle-size discretization; and the number of conversion states depends on the conversion mechanisms considered. Thus, the structure proposed provides sufficient flexibility to accommodate different boiler configurations and varying levels of model complexity.

3.4.3 Numerical Solution Strategy

The system of coupled ODEs is solved using SciPy's solver, **solve_ivp**. Different time-marching methods were tested to assess the system's stiffness characteristics and identify the most suitable solution strategy [36]. Explicit methods based on Runge-Kutta formulations showed poor numerical performance due to the stiff nature of the system. Among the implicit methods available, the BDF method provided the most robust performance. Other implicit methods, such as Radau and LSODA, did not provide significant improvements in computational cost or solution accuracy, even for the most complex model configuration.

The BDF method employs adaptive time-stepping and controls the truncation error through absolute and relative tolerances. These tolerances can be adjusted to achieve stable solutions at an acceptable computational cost. For the majority of the simulations, a baseline tolerance configuration was adopted to provide increased localized accuracy in regions exhibiting larger gradients, specifically within the dense bed tracking layers. This baseline configuration consisted of a relative tolerance, **rtol**, of 10^{-5}, and an absolute tolerance, **atol**, of 10^{-5} for all layers and a stricter value of 10^{-6} for the dense bed region. Together with these tolerances, the dense bed tracking tolerance, δ, was chosen between the range of 10^{-4} and 10^{-5}. In cases involving more demanding model configurations with stronger stiffness or fast solution variations, stricter tolerances were employed to improve solver stability and performance.

3.4.3.1 Computational Measures

Additional computational measures were implemented to improve numerical performance. Apart from vectorized formulations using Boolean indexing to reduce the excessive use of conditional statements and iterative operations, arrays used for calculation were preallocated and reused to avoid repeated memory allocation.

Furthermore, fuel and secondary air injection were introduced sequentially after a first steady-state hydrodynamic condition was achieved. This measure was adopted

to reduce abrupt changes in the variables and avoid excessive model stiffness. A smooth injection profile was implemented in both cases to allow a gradual transition towards a constant injection rate. The injection profile was expressed as:

$$I(t, \tau_i) = R_i \left(1 - e^{-\frac{t-t_0}{\tau_i}}\right) \tag{3.30}$$

where R_i is the injection rate, t_0 is the starting time of injection, and τ_i is the injection characteristic time, with larger values of the characteristic time producing more gradual transitions.

3.5 Numerical Checking

3.5.1 Test Matrix

Mesh sensitivity studies were performed to evaluate the variability and stability of the solution with different mesh configurations. Three study groups, summarized in the tables below, were defined to study the effect of the mesh resolution (group A), fine-layer distribution (group B), and coarse-to-fine layer height ratio (group C) on the solution of the system.

The studies were first performed using only the hydrodynamics model, since the solids transport formulation determines the numerical stability of the complete model. Mesh configurations exhibiting unstable solution behavior or high computational cost, even after applying stricter error tolerances, were excluded from further testing. The most stable meshes were subsequently evaluated with the inclusion of secondary air and fuel conversion to verify that numerical stability and solution consistency were maintained under more complex conditions.

Case	Fine Layers	Coarse Layers	Total Layers	Height Ratio
A1 Coarse	18	12	30	4
A2 Medium	24	16	40	4
A3 Baseline	30	20	50	4
A4 Fine	36	24	60	4
A5 Very Fine	42	28	70	4

Table 3.2: Group A Mesh Configurations, to study the effect of the mesh resolution.

Case	Fine Layers	Coarse Layers	Total Layers	Height Ratio
B1 Low	15	35	50	4
B2 Balanced	25	25	50	4
B3 Baseline	30	20	50	4
B4 High	35	15	50	4
B5 High	40	10	50	4

Table 3.3: Group B Mesh Configurations, to study the effect of the fine-layer distribution near the dense bed region.

Case	Fine Layers	Coarse Layers	Total Layers	Height Ratio
C1	30	20	50	2
C2	30	20	50	3
C3 Baseline	30	20	50	4
C4	30	20	50	6
C5	30	20	50	8

Table 3.4: Group C Mesh Configurations, to study the effect of the coarse-to-fine layer height ratio.

3.5.2 Results

Figure 3.8 and the tables below summarize the initial mesh studies employing only the hydrodynamics formulation, using an identical model configuration for consistency. The performance metrics shown in Figure 3.8 were retrieved using Python profiling tools. The number of Jacobian evaluations is directly related to the solution process of the BDF method, indicating the frequency at which the solver updates the Jacobian matrix to account for changes in the system dynamics, typical under increased stiffness or strong gradients in the solution. In mesh configurations where the dense bed jumped to adjacent layers, the number of Jacobian evaluations increased.

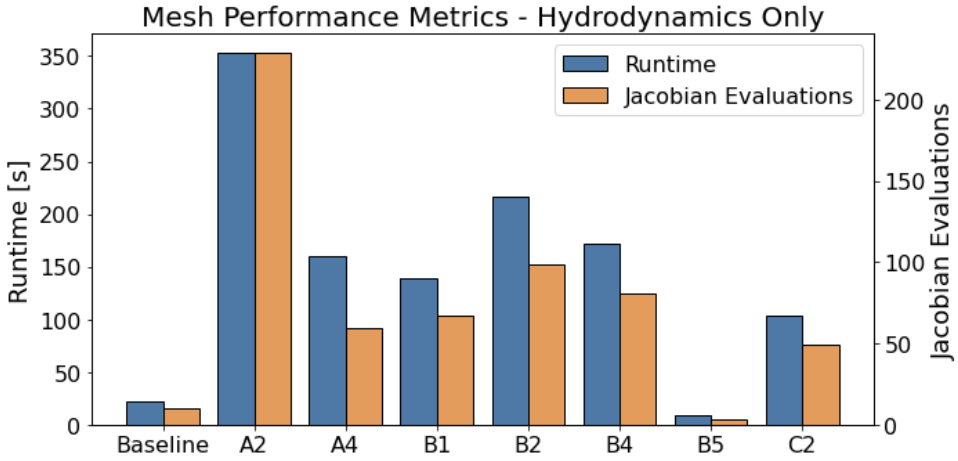

Figure 3.8: Performance metrics for all converged meshes after hydrodynamics-only runs.

The behavior of group A suggests a stable solution region for a total cell count between 40 and 60 layers. Figure 3.9 shows the temporal evolution of the dense bed height during the first 500 seconds of simulation for the successful mesh configurations in group A. All three meshes reached similar steady-state solutions, exhibiting differences no bigger than 5 mm. Furthermore, the results indicate that dense bed jumping does not significantly affect the dense bed evolution or the final steady-state solution. However, the presence of dense bed jumps noticeably increased the computational cost. Comparing the fine mesh A4 with the baseline mesh A3, the computational time increased by approximately a factor of five.

Mesh	Status	rtol	atol local	atol general	δ	Notes
A1	Not converged	10^{-5}	10^{-6}	10^{-5}	10^{-4}	Early stop.
A2	Converged	10^{-5}	10^{-6}	10^{-5}	10^{-4}	No dense bed jump.
A3	Converged	10^{-5}	10^{-6}	10^{-5}	10^{-4}	Baseline. No dense bed jump.
A4	Converged	10^{-6}	10^{-7}	10^{-6}	10^{-6}	Dense bed jumped. Stricter tolerances.
A5	Not Converged	10^{-7}	10^{-8}	10^{-7}	10^{-6}	Failed under stricter tolerances.

Table 3.5: Group A results with error tolerances and remarks.

Mesh	Status	rtol	atol local	atol general	δ	Notes
B1-B4	Converged	10^{-5}	10^{-6}	10^{-5}	10^{-4}	Dense bed jumped.
B3	Converged	10^{-5}	10^{-6}	10^{-5}	10^{-4}	Baseline. No dense bed jump.
B5	Converged	10^{-5}	10^{-6}	10^{-5}	10^{-4}	Fastest case. No dense bed jump.

Table 3.6: Group B results with error tolerances and remarks.

Mesh	Status	rtol	atol local	atol general	δ	Notes
C1	Not converged	10^{-5}	10^{-6}	10^{-5}	10^{-4}	Insufficient refinement.
C2	Converged	10^{-5}	10^{-6}	10^{-5}	10^{-4}	Dense bed jumped.
C3	Converged	10^{-5}	10^{-6}	10^{-5}	10^{-4}	Baseline. No dense bed jump.
C4	Not Converged	10^{-7}	10^{-8}	10^{-7}	10^{-6}	Failed under stricter tolerances.
C5	Not Run	–	–	–	–	Skipped

Table 3.7: Group C results with error tolerances and remarks.

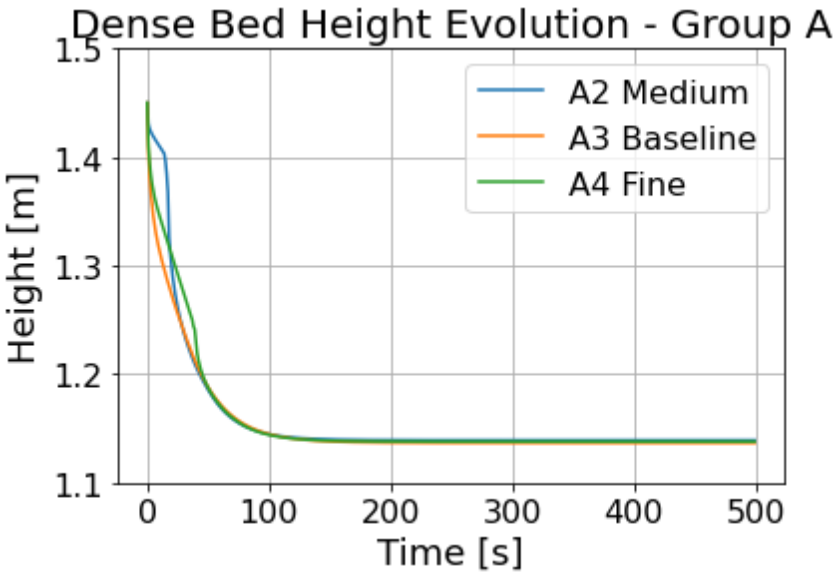

Figure 3.9: Dense bed height evolution for group A mesh configurations

Figure 3.10 summarizes the dense bed evolution for group B. Similar to group A, most mesh configurations reached similar steady-state solutions, with mesh B1 having a noticeable deviation in the final dense bed height. Although the difference remained within millimetric range, the results suggest the existence of a minimum fine-layer threshold beyond which further refinement produces minor changes in the steady-state solution. The results also follow the trend observed for group A, where dense bed jumps primarily affected the computational time rather than the steady-state solution, reaching in some cases computational times up to 7 times longer than the baseline. Interestingly, the configuration with the highest fine-layer count, B5, had the shortest computational time of approximately 8 seconds.

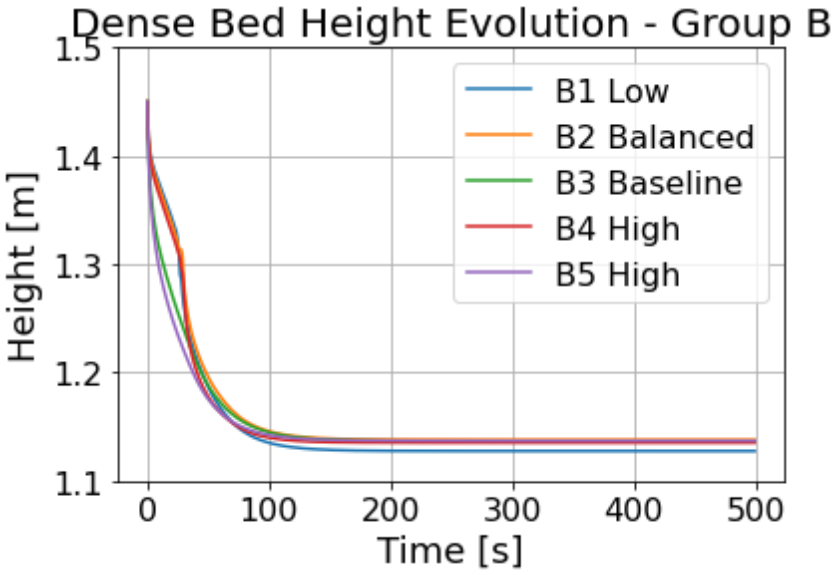

Figure 3.10: Dense bed height evolution for group B mesh configurations

Figure 3.11 summarizes the dense bed evolution for the only two successful mesh cases in group C. These results further confirm the trends observed in the previous groups. Additionally, the results suggest that solution stability has a high sensitivity to the layer-height ratio, with only two configurations achieving stable solutions. It should be noted that the mesh configuration providing the most stable performance may vary depending on the operating conditions and model inputs. The results of group C suggest that, for the conditions used in the present study, height ratios below 3 and above 4 may lead to unstable numerical behavior. However, this observation is not necessarily a general criterion, since the optimal height ratio, and also the total mesh resolution and fine-layer distribution, may depend on the operating case being analyzed.

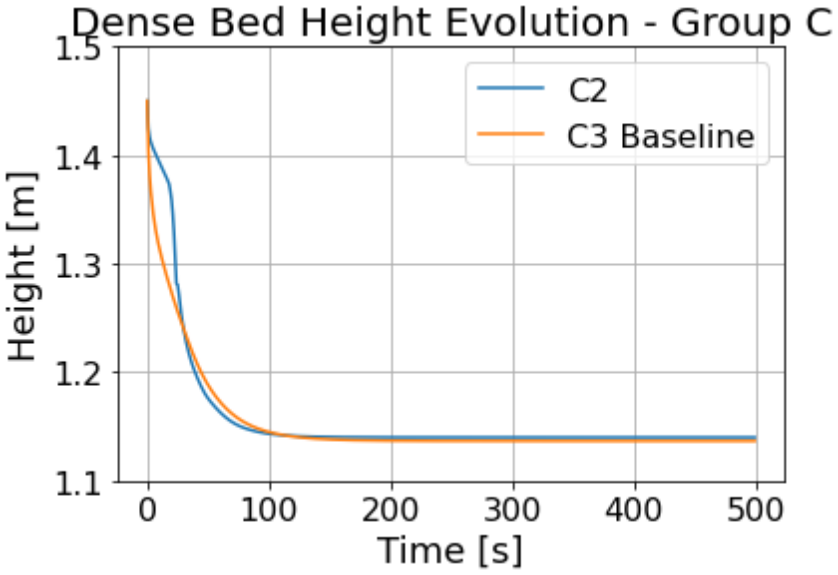

Figure 3.11: Dense bed height evolution for group C mesh configurations

Overall, the mesh sensitivity studies indicate that numerical stability depends on a combined interaction between the coarse-to-fine layer height ratio, mesh resolution, and fine-layer count. From the analyzed parameters, the height ratio exhibited the strongest influence on solution stability, while the refinement and resolution primarily affected the computational cost. From the analyzed meshes, only the baseline case and configuration B5 were run with the full model, combining solids hydrodynamics with secondary air injection and fuel conversion. Similar steady-state solutions to the ones indicated above were reached, so the primary comparison between the two full runs is done from a performance perspective.

Figure 3.12 summarizes the performance metrics for the two configurations studied. Despite B5 having a computational time approximately 3 times shorter than the baseline, the computational cost of both configurations is very similar when the full model formulation is used. These results also suggest that mesh configurations in which the hydrodynamics do not exhibit dense bed jumps can still experience high computational costs when running the full model, indicating that fuel conversion

and secondary air have an important effect on computational time. This behavior can be attributed to the increased size of the matrices used in the full model to account for additional particle states and source terms, together with the transient effects from secondary air and fuel injection that can increase the stiffness of the system.

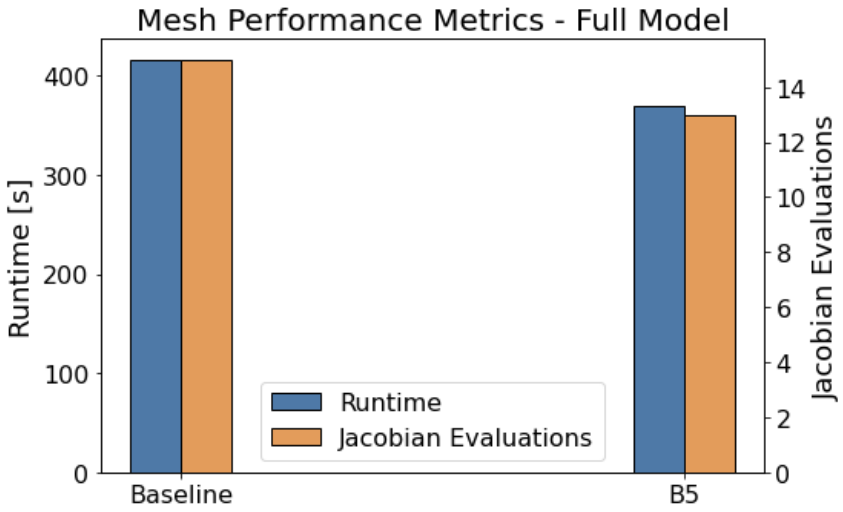

Figure 3.12: Performance metrics for full-model runs.

Based on the combined assessment of numerical stability, solution consistency, and mesh refinement for both the dense and freeboard regions, the baseline mesh configuration was selected for the remaining simulations. This configuration provided stable dense bed behavior, acceptable computational cost, and adequate spatial resolution. Any mesh modifications introduced for specific cases will be described accordingly in the Results chapter.

3.6 Model Runs and Validation

3.6.1 Validation Procedure

The solids hydrodynamics model was validated using two large-scale boilers as reference systems: HOFOR's 500 MW CFB Boiler in Copenhagen for district heating and electricity generation, and Chalmers' 12 MW CFB boiler at Kraftcentralen for district heating. Validation was performed primarily through comparison of the vertical solids concentration distributions and circulation rates, since these quantities directly reflect the hydrodynamic behavior captured in the present model.

Four solids concentration measurements at different heights are available for the HOFOR boiler, together with the solids circulation at the cyclone exit at the top of the furnace. The concentration values were estimated from the pressure measurements during a period of stable operation at constant load between November 2025 and January 2026. These measurements were compared against the concentration profile predicted by the model and the calculated solids circulation at the uppermost

discretization layer.

Solids concentration profiles and PSDs from the Chalmers boiler were obtained from the experiments on solids vertical distribution carried out by Johnsson and Leckner for two operational cases [27]. The experimental measurements were compared against the solids concentration profile predicted by the model.

Figure 3.13 presents the PSDs for the bed material in each of the analyzed boilers. Furthermore, the tables below summarize the operating conditions and relevant model inputs employed in the simulations for both boilers[1], including validation. Any deviation from the operating conditions listed below is described in the corresponding Results section.

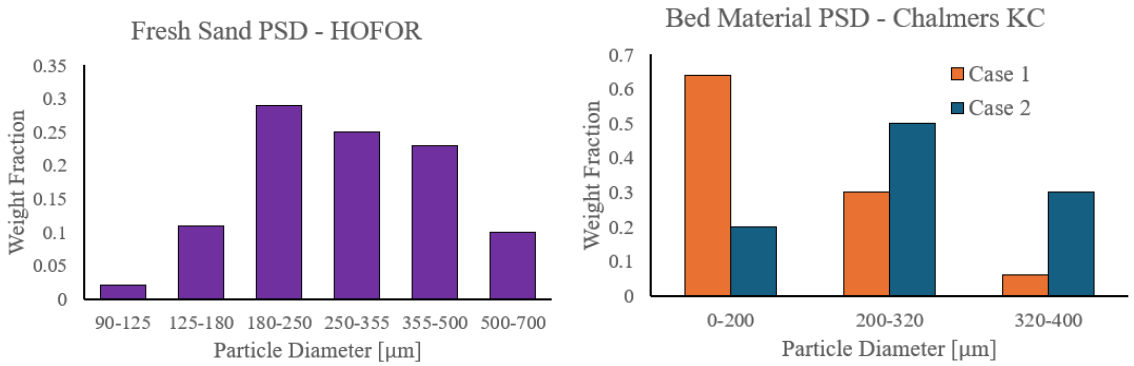

Figure 3.13: PSDs for HOFOR and Chalmers, used for all corresponding model runs.

Parameter	Value
Primary air velocity, u_g [m/s]	2.5
Secondary air velocity [m/s]	2.5
Air density, ρ_g [kg/m^3]	0.33
Air viscosity, μ_g [Pa·s]	4.3e-5
Secondary air velocity [m/s]	2.5
Velocity at the wall layer, u_w [m/s]	8
Maximum solids fraction, ε_g	0.65
Initial bed height [m]	1.1
Particle density of sand, ρ_s [kg/m^3]	2600
Fuel injection rate [kg/s]	30
Wet biomass particle density [kg/m^3]	500
Wet biomass initial size [mm]	20

Table 3.8: Baseline inputs for model runs in the HOFOR Boiler

[1]Exact HOFOR system dimensions are not disclosed due to company confidentiality. The Chalmers KC dimensions and additional operating parameters were obtained from Tove Djerf's PhD Thesis [3].

Parameter	Value
Primary air velocity, u_g [m/s]	2.7
Secondary air velocity [m/s]	0
Air density, ρ_g [kg/m^3]	0.33
Air viscosity, μ_g [Pa·s]	4.3e-5
Velocity at the wall layer, u_w [m/s]	8
Maximum solids fraction, ε_g	0.65
Initial bed height [m]	0.58
Particle density of sand, ρ_s [kg/m^3]	2600

Table 3.9: Baseline inputs for model runs in the Chalmers KC Boiler

3.6.2 Sensitivity Analysis of Operating Conditions and Model Parameters

A sensitivity study was conducted to evaluate the influence of operating conditions and model parameters on the predicted system behavior.

The primary and secondary air velocities were varied to analyze their effect on the vertical distribution of solids and circulation rates. These studies were performed using HOFOR's boiler operating conditions and geometry. Three primary air velocities, 1.5, 2.5, and 3 m/s, were evaluated using the hydrodynamics model, neglecting the effects of secondary air injection and fuel conversion. Subsequently, three secondary air flowrates corresposnding to superficial velocities of 0, 1, and 2.5 m/s, were compared while maintaining a constant primary air velocity of 2.5 m/s and neglecting the effect of fuel conversion.

Additionally, the influence of the lateral transport intensity was analyzed. Three lateral transport multipliers, 2, 4, and 5, were compared against the baseline case without a multiplier. The comparison was done through the vertical concentration distributions predicted by the model, while maintaining the primary and secondary superficial air velocities at 2.5 m/s.

Finally, the effect of fuel composition was evaluated using a biomass composition with higher initial moisture (30%) and reduced volatile content (58%). It was assumed that the additional moisture increased the drying characteristic time, τ_1, to 40 s, and reduced the devolatilisation characteristic time, τ_2, to 20 s. These conversion sensitivity studies were evaluated through comparisons of conversion evolution curves.

4

Results and Discussion

4.1 Model Validation

4.1.1 HOFOR Boiler

Figure 4.1 shows the steady-state solids concentration profile for the HOFOR boiler together with the experimental validation points and their corresponding error bars.

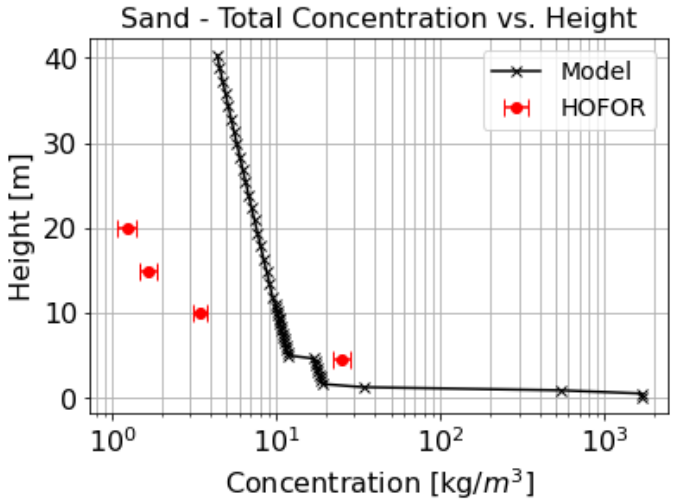

Figure 4.1: Vertical solids concentration profile for the HOFOR boiler.

The predicted profile shows an overestimation of the actual solids concentration in the freeboard, and a slight underestimation of the solids concentration near the upper secondary injection level. The discrepancy between modeled and experimental values might be associated with the effective solids inventory in the riser and the simplifications applied to the recirculation flux passing through the cyclone and loop seal. In large CFBs such as the HOFOR unit, most of the solids inventory is contained within the loop seal, accumulating mainly the finer particles that are more easily entrained from the dense bed. In the present model, the transport of particles from the furnace exit to the lower regions is assumed to happen instantaneously, neglecting the residence time and accumulation effects inside the particle seal. Thus, the progressive reduction of finer particle concentrations in the riser is not captured in the model, maintaining a regular entrainment flow from the dense bed and contributing to the overprediction of the freeboard concentration.

Figure 4.2 presents the detailed concentration profiles for the individual particle size classes within the PSD given in Figure 3.13, and the corresponding temporal evolution of the average particle diameter distribution in the furnace. The results indicate that the freeboard is primarily occupied by finer particles, which are more easily entrained by the gas flow, decreasing the average particle diameter to approximately 160 μm at steady state. In industrial boilers, the entrained particles pass through the cyclone and the particle seal before returning to the furnace. This leads to a progressive reduction of fine particle fraction in the riser's inventory, and a higher concentration of larger particles in the dense region. As larger particles have higher terminal velocities and lower entrainment tendencies, the solids concentration entrained into the freeboard decreases, which is consistent with the trend observed in the HOFOR measurements.

In addition, the overprediction of the solids concentration leads to an overprediction of the solids circulation, with a predicted value of 18.62 kg/m^{2}s versus an experimental value of 2.9 kg/m^{2}s under high-load conditions.

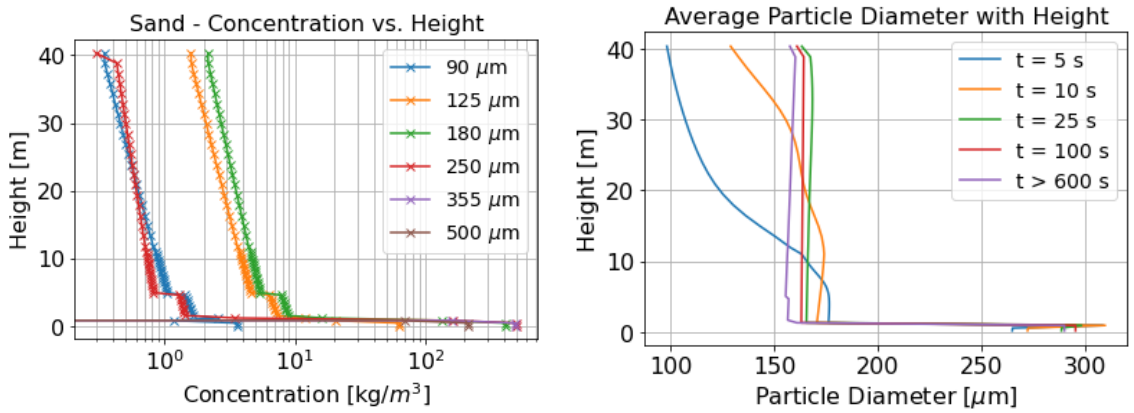

Figure 4.2: Detailed solids concentration profile for each size class at steady state (left) and temporal evolution of the average particle size with height (right) for the HOFOR boiler.

Furthermore, the validation points suggest a steeper decay of the freeboard concentration than predicted by the model. This may suggest an underestimation of the interior area on which the wall layers form, leading to an underestimation of the lateral transport magnitude. Lower lateral transport of particles to the wall layers increases the residence time of the solids in the core region, leading to higher predicted concentrations in the freeboard. The influence of lateral transport parameters is further examined in subsequent sections.

4.1.2 Chalmers Boiler

Figure 4.3 shows the predicted solids concentration profiles for the Chalmers KC boiler together with the experimental data points. The predicted concentration distributions show good agreement with the experimental measurements, reproducing both the dense region concentrations and the observed transport zone decay. In

addition, the agreement with the experimental points in the dense region suggests a reasonably good prediction of the dense bed level under steady-state conditions.

Some discrepancy can be observed in the solids concentration between 1 and 2.5 m. This deviation may primarily be associated with the assumptions and simplifications adopted for the splash zone modeling, where the presence of solid clusters and strong back-mixing can increase the local solids concentrations beyond the values predicted by the model.

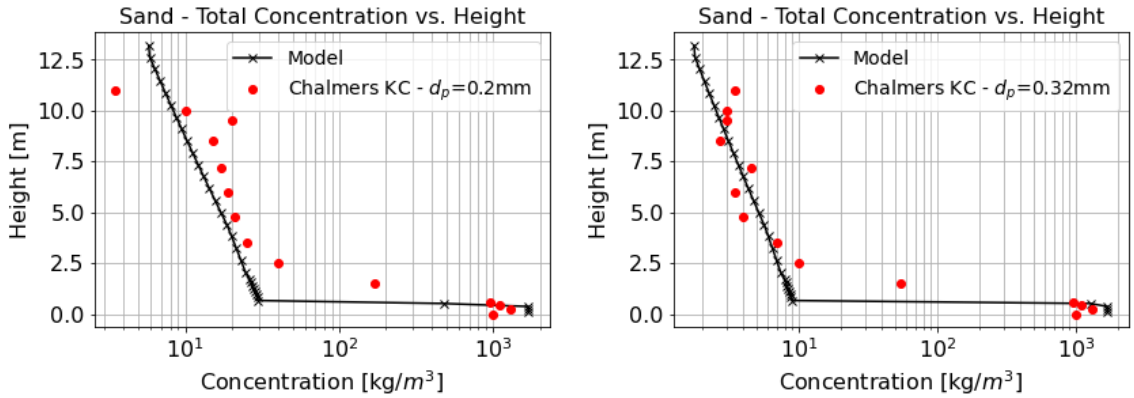

Figure 4.3: Predicted solids concentration profiles for the two analysis cases with different PSDs for the Chalmers KC boiler

Furthermore, the close agreement observed in the transport zone decay may partly be related to the formulation of Equation 2.19, since the semi-empirical correlation was developed using data from the Chalmers KC boiler and other industrial and laboratory-scale units. Consequently, the correlation may provide a more representative description of the lateral transport behavior for this system.

4.2 Influence of Operating Conditions and Model Parameters

4.2.1 Primary Air Velocity

Figure 4.4 compares the dense bed evolution and solids concentration profiles between the three primary air velocity cases.

The dense bed evolution exhibits a clear dependence on the primary air velocity, with higher primary air velocities resulting in lower dense bed levels in steady-state conditions. This behavior is consistent with fluidization physics, since increasing the gas flow entering the furnace enhances solids entrainment from the dense bed and increases the solids concentration in the freeboard, as shown by the predicted profiles. The trend also suggests that sufficiently high primary air velocities may significantly reduce the size of the dense region.

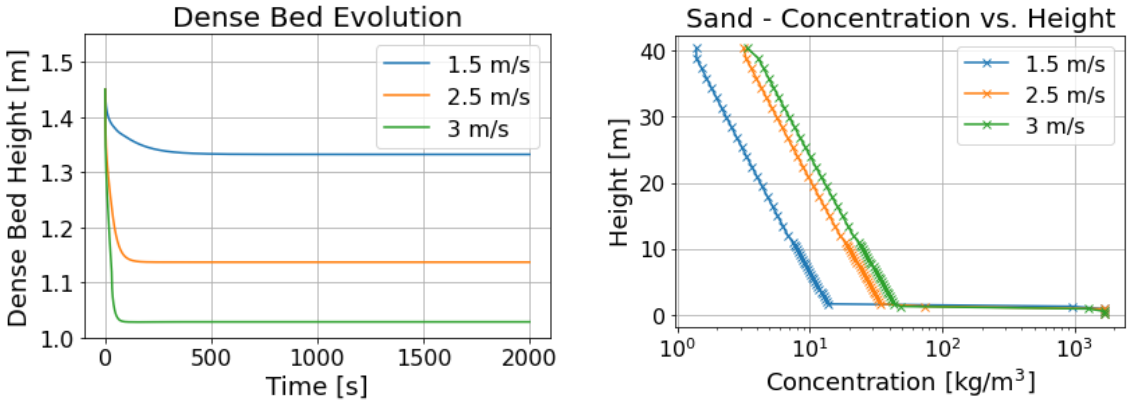

Figure 4.4: Predicted dense bed evolutions (left) and solids concentration profiles (right) for different values of primary air velocity.

This behavior is further corroborated by Figure 4.5, showing an increase in the average particle diameter with higher primary air velocities. Higher gas velocities increase the carrying capacity of the gas phase and enable larger particles to become entrained into the upper regions of the furnace. Solids circulation at the furnace outlet also exhibits an increase with higher primary air velocities, from 1.28 kg/m^{2}s at 1.5 m/s to 7.44 kg/m^{2}s at 3 m/s, which is consistent with the enhanced entrainment of particles.

Furthermore, both the dense bed evolution curves and average diameter contours show a faster system stabilization at higher primary air velocities, reaching steady-state conditions earlier than the lower velocities.

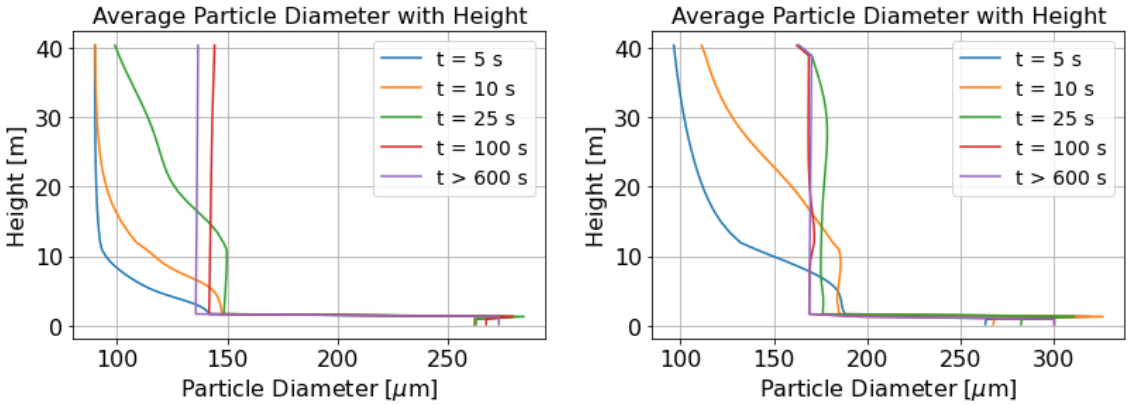

Figure 4.5: Evolution comparison of the average particle diameter distribution for primary velocities of 1.5 m/s (left) and 3 m/s (right).

4.2.2 Secondary Air Velocity

Figure 4.6 compares the dense bed evolution and solids concentration profiles for the three secondary air velocity cases. Secondary injection was introduced for all cases at $t = 400s$, with a characteristic injection time of 50 s.

The dense bed evolution curves show an interesting behavior, with dense bed level increasing with higher secondary air velocities. This behavior may be associated with changes in the solids circulation patterns. The additional gas flow above the injection heights increases particle transport and enhances lateral migration to the wall layers, increasing the downward recirculation of solids toward the dense region. This behavior is further explained by the concentration profiles, indicating more gradual decays in the transport zone as the secondary air velocity increases, while simultaneously showing lower solids concentrations in the core region at lower heights, suggesting the enhancement of lateral migration into the wall layers.

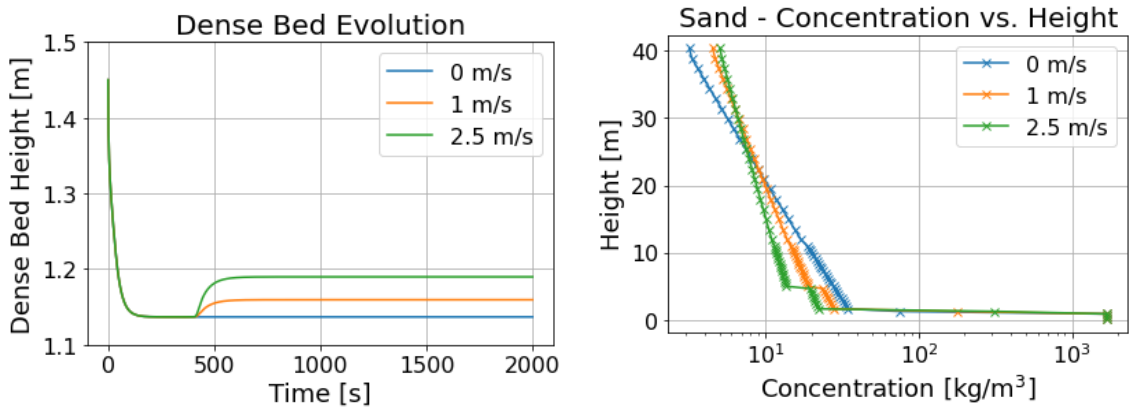

Figure 4.6: Predicted dense bed evolutions (left) and solids concentration profiles (right) for different values of secondary air velocity.

Furthermore, increasing the secondary air velocity leads to a substantial increase in the solids circulation, going from 5.57 kg/m^{2}s to 21.59 kg/m^{2}s with a secondary air superficial velocity of 2.5 m/s. The larger gas flow above the injection heights carries more solids to the top of the boiler, which may explain the increase in solids circulation at the furnace outlet.

4.2.3 Lateral Transport

Figure 4.7 shows the dense bed evolution curves and solids concentration profiles for different lateral transport multipliers.

The evolution of the dense bed height follows an interesting behavior. As the lateral transport multiplier increases, the dense bed growth effect induced by the secondary air injection is progressively attenuated. For sufficiently high multiplier values, the dense bed level even decreases after the secondary air introduction.

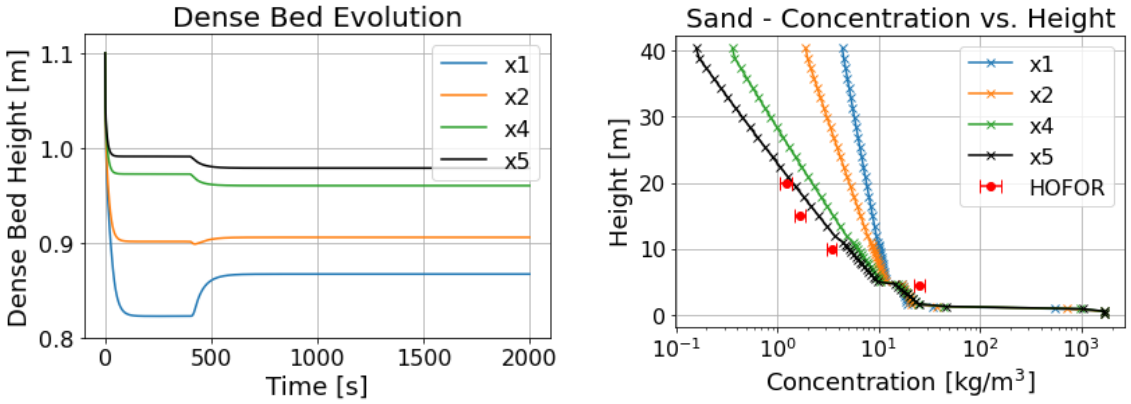

Figure 4.7: Predicted dense bed evolutions (left) and solids concentration profiles (right) for different magnitudes of lateral transport.

Enhanced lateral transport increases particle migration from the core region toward the wall layers, reducing the solids residence time in the core and promoting recirculation to denser regions in the lower furnace. The concentration profiles further reinforce this theory, as fewer particles remain suspended in the core region, leading to lower predicted solids concentrations. Figure 4.8 shows an additional trend, with average particle diameter increasing with height, at steady state, when the lateral transport is enhanced. This suggests that finer particle sizes concentrate at the bottom regions and do not reach higher elevations due to stronger lateral migration into the wall layers and recirculation to the denser regions.

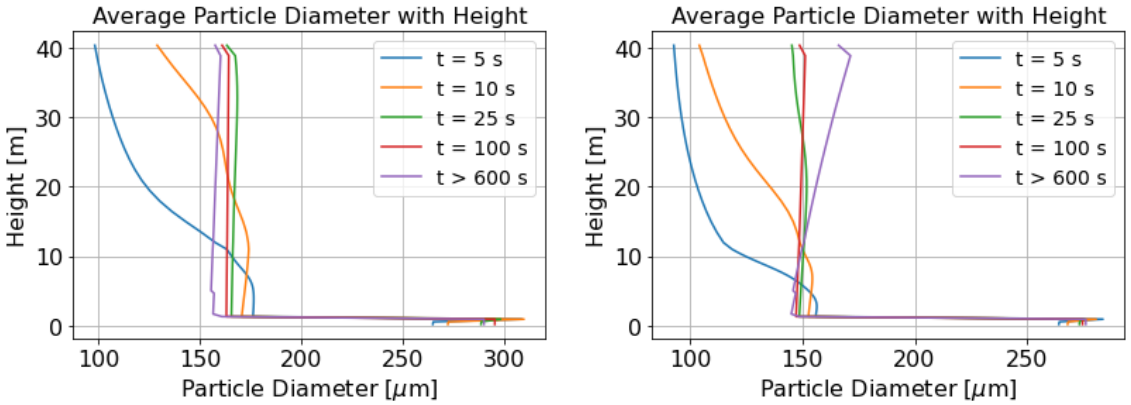

Figure 4.8: Average particle diameter evolution for a multiplier of 1 (left) and a multiplier of 5 (right).

The concentration profiles also suggest that, for a certain multiplier value above 5, the predicted concentration profile exhibits a better agreement with the experimental values for the HOFOR case, supporting the hypothesis that the lateral transport area may be underestimated in the geometrical representation of the current model. Furthermore, the solids circulation decreases considerably, dropping from 18.62 kg/m^{2}s at a multiplier of 1 to 0.66 kg/m^{2}s at a multiplier of 5, indicating a substantial reduction in solids transport toward the furnace outlet.

4.3 Fuel Conversion

Figure 4.9 summarizes the fuel conversion predictions with the present model. Fuel injection is initiated at $t = 600s$, with a characteristic injection time of 30 s.

Based on the fuel composition with a low initial moisture and high volatile content, the conversion evolution shows an accumulation of dry biomass over time. This behavior is consistent with drying occurring at a faster rate than devolatilisation, leading to a temporary build-up of dry biomass before further conversion into char.

The size reduction of the fuel particles during drying and devolatilisation causes the produced char particles to become increasingly entrained by the gas flow and distribute along the furnace height. However, with the given biomass composition and shrinkage rates, the attained char size and density lead to a relatively high particle terminal velocity. Consequently, char particles' vertical concentration distribution is very low, with most of the char concentrated in the dense region. Char combustion becomes vertically distributed in the furnace as a consequence of the entrainment of a fraction of the char particles. However, the combustion source term remains stronger in the dense bed region due to larger solids concentration and higher char inventory. The drying and devolatilisation source terms take place primarily in the dense region, since wet and dry biomass particles retain larger diameters and higher particle densities, making them less prone to entrainment.

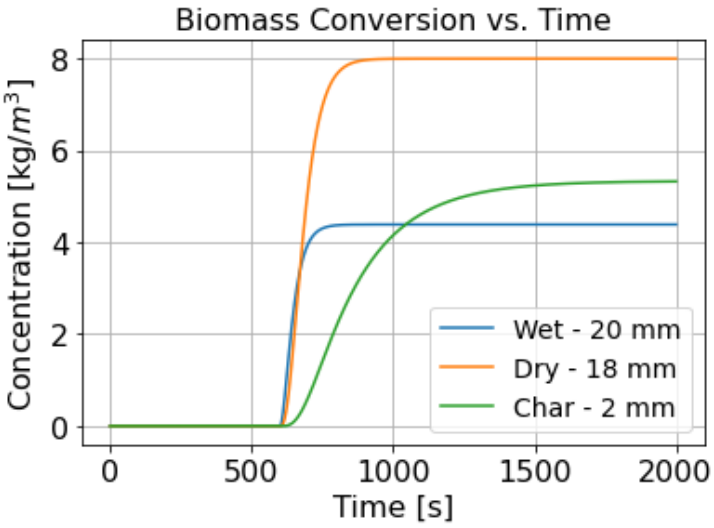

Figure 4.9: Predicted fuel conversion evolution.

Figure 4.10 shows the effect of modifying the fuel composition on the conversion evolution. The increased drying time required increases the concentration of wet biomass in the system. Consequently, the shorter devolatilisation time leads to faster char formation, increasing the magnitude and spatial distribution of the combustion source term. However, char combustion is still primarily concentrated in the dense bed regions, highlighting the importance of maintaining a dense bed in CFB units to improve fuel conversion.

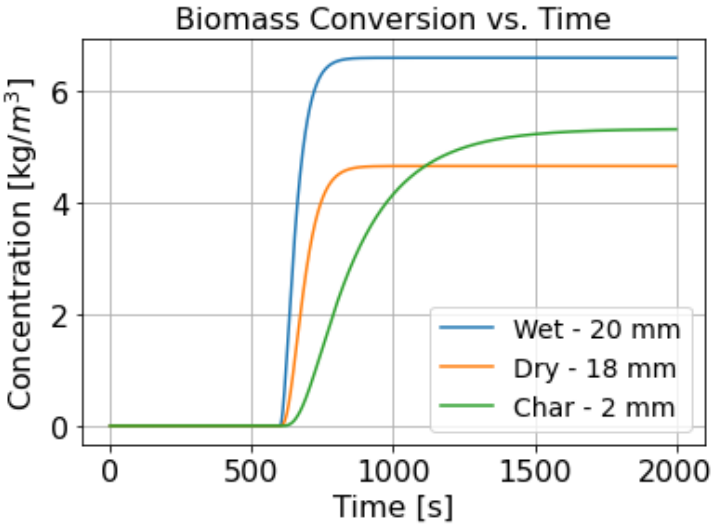

Figure 4.10: Predicted fuel conversion evolution for a biomass composition with 30% initial moisture and 58% volatile content.

5

Conclusions and Future Work

A transient semi-empirical 1.5D model for biomass-fired CFB boilers was developed to predict the hydrodynamic and fuel conversion behavior of large-scale units. The model coupled solids transport formulations with fuel conversion mechanisms and was validated against experimental data from industrial systems. The results showed that the proposed approach produced physically-consistent behaviors while maintaining computational efficiency. The main takeaways of the model development and testing are listed below:

- The validation against the HOFOR and Chalmers KC boilers revealed the importance of accounting for the solids inventories in the return leg, as their neglect results in considerable error in systems where a large share of the solids is contained in the particle seal. However, the general qualitative consistency of the results across units with different geometrical configurations and operating conditions indicates a satisfactory degree of adaptability and generalization of the model framework.
- The sensitivity studies demonstrated a strong dependence of the predicted hydrodynamic behavior on gas velocities and lateral transport mechanisms. Primary air velocity significantly influenced solids entrainment and circulation rates, while secondary air modified solids recirculation and dense bed evolution.
- Lateral transport sensitivity studies showed that, under higher lateral migration of particles to the wall layers, the concentration profiles reach a better level of agreement with the experimental data for the HOFOR boiler, supporting the hypothesis that the current geometrical representation underestimates the effective lateral transport area.
- Fuel conversion predictions indicated that particle shrinkage and fuel composition changes strongly affect the spatial distribution of the conversion stages. Char particles became progressively entrained due to their reduced particle diameter, resulting in vertically distributed combustion, which remained stronger in the dense bed region.
- The model's computational efficiency is dependent on the system's stiffness and transient behavior. Events such as dense bed jumps to adjacent layers or injection curves can increase the stiffness of the system, leading to increased computational time. A good balance between accuracy and spatial discretization, together with temporal staging of transient events, was found to be a good approach to maintain computational efficiency with adequate solution stability.
- The proposed data architecture proved effective for variable handling and

model formulation. The use of 5D arrays enabled flexible management of solution quantities for different solids families and conversion states.

The model developed in the present work can be further refined to achieve a more complete representation of large-scale CFB operation. A natural continuation in the modeling work is the introduction of the gas phase balancing and gas species transport. Such formulations would allow a tighter interaction between fuel conversion and hydrodynamics and provide the necessary framework for heat transfer modeling.

The model is able to capture the dynamic behavior of CFB systems, tracking the dense bed evolution with time. However, the tracking approach can still be further improved to tackle the dense bed jumping effects on computational efficiency and solution stability. The movement of the dense bed between layers increases system stiffness and affects computational efficiency, making the tracking approach the main computational bottleneck. Future developments should focus on improving the dense bed tracking methodology to reduce the effects of dense bed jumps while maintaining solution stability.

Furthermore, formulations for the recirculation loop, i.e. the cyclone and particle seal, need to be included to attain more realistic solids distribution profiles. As was observed with the validation results, the effective solids inventory in the riser is overestimated, leading to an overprediction in the solids concentrations and circulation. An adjustment of the particle seal definition, introducing prolonged permanence of finer particles inside the seal, can improve the prediction of the effective inventory in the furnace.

Finally, the model's fuel conversion module is still in early development. Despite being capable of interacting with the hydrodynamics module, showing fuel mixing within the dense bed and char entrainment in the freeboard, the results can still become more realistic and industrially relevant through more robust formulations. Additional inputs to the model, like fuel PSDs and improved considerations on particle size evolution during conversion (such as multiple char size classes), could aid in achieving more industrially relevant results.

Bibliography

[1] H. Wang et al. "Vision article: new advances in gas-solids fluidized beds for novel thermochemical reaction processes and energy storage". In: *Applied Thermal Engineering* 297 (2026), p. 130820. ISSN: 1359-4311. DOI: https://doi.org/10.1016/j.applthermaleng.2026.130820. URL: https://www.sciencedirect.com/science/article/pii/S1359431126011282.

[2] G. Martinez Castilla. "Fluidized bed plants for heat and power production in future energy systems". PhD thesis. Göteborg, Sweden: Chalmers University of Technology, 2023. ISBN: 978-91-7905-923-1.

[3] T. Djerf. "Solids Flow in Large-Scale Circulating Fluidized Bed Furnaces". PhD thesis. Göteborg, Sweden: Chalmers University of Technology, 2021. ISBN: 978-91-7905-511-0.

[4] S. Sungworagarn, P. Sathitruangsak, and T. Madhiyanon. "CFB Combustion of alkali-laden biomass: Agglomeration and fouling resistance". In: *Results in Engineering* 27 (2025), p. 105999. ISSN: 2590-1230. DOI: https://doi.org/10.1016/j.rineng.2025.105999. URL: https://www.sciencedirect.com/science/article/pii/S2590123025020717.

[5] Y. Wang and J. J. Wu. "Thermochemical conversion of biomass: Potential future prospects". In: *Renewable and Sustainable Energy Reviews* 187 (2023), p. 113754. ISSN: 1364-0321. DOI: https://doi.org/10.1016/j.rser.2023.113754. URL: https://www.sciencedirect.com/science/article/pii/S1364032123006111.

[6] J.-P. Hannes. "Mathematical Modelling of Circulating Fluidized Bed Combustion". PhD thesis. Aachen, Germany: Delft University of Technology, 1996. ISBN: 3-88817-002-8.

[7] D. Pallarès and F. Johnsson. "Macroscopic modelling of fluid dynamics in large-scale circulating fluidized beds". In: *Progress in Energy and Combustion Science* 32.5 (2006), pp. 539–569. ISSN: 0360-1285. DOI: https://doi.org/10.1016/j.pecs.2006.02.002. URL: https://www.sciencedirect.com/science/article/pii/S0360128506000360.

[8] W. Wang et al. "A review of multiscale CFD for gas–solid CFB modeling". In: *International Journal of Multiphase Flow* 36.2 (2010). Special Issue: Multiphase Flow Research in China, pp. 109–118. ISSN: 0301-9322. DOI: https://doi.org/10.1016/j.ijmultiphaseflow.2009.01.008. URL: https://www.sciencedirect.com/science/article/pii/S0301932209000184.

[9] A. Köhler. "Mixing of Large Solids in Fluidized Beds: Semiempirical Modeling and Experiments with Application to Fuel Mixing". PhD thesis. Gothenburg, Sweden: Chalmers University of Technology, 2021. ISBN: 978-91-7905-509-7.

[10] C.hangwon Yang et al. “One-dimensional numerical simulation of CFB combustion: Improvement of hydrodynamic models for accurate prediction of pressure and particle size distributions”. In: *Fuel* 346 (2023), p. 128315. ISSN: 0016-2361. DOI: https://doi.org/10.1016/j.fuel.2023.128315. URL: https://www.sciencedirect.com/science/article/pii/S0016236123009286.

[11] X. Bi J. R. Grace and N. Ellis, eds. *Essentials of Fluidization Technology*. Weinheim, Germany: Wiley-VCH, 2020. ISBN: 978-3-527-34064-4.

[12] K. Win et al. “Transport Velocity of Coarse Particles in Multi-Solid Fluidized Bed”. In: *Journal of Chemical Engineering of Japan - J CHEM ENG JPN* 28 (Oct. 1995), pp. 535–540. DOI: 10.1252/jcej.28.535.

[13] D. Geldart. “Types of gas fluidization”. In: *Powder Technology* 7.5 (1973), pp. 285–292. ISSN: 0032-5910. DOI: https://doi.org/10.1016/0032-5910(73)80037-3. URL: https://www.sciencedirect.com/science/article/pii/0032591073800373.

[14] D. Kunii and O. Levenspiel. *Fluidization Engineering*. 2nd ed. Boston: Butterworth-Heinemann, 1991. ISBN: 0-409-90233-0.

[15] S. Mahmoudi et al. “Solids flow diagram of a CFB riser using Geldart B-type powders”. In: *Particuology* 10.1 (2012), pp. 51–61. ISSN: 1674-2001. DOI: https://doi.org/10.1016/j.partic.2011.09.002. URL: https://www.sciencedirect.com/science/article/pii/S1674200111001908.

[16] S. Zhang et al. “Axial behavior of Geldart B particles in an ultra-complex 3D structure using distributed ECVT with 96 electrodes”. In: *Chemical Engineering Journal* 525 (2025), p. 170404. ISSN: 1385-8947. DOI: https://doi.org/10.1016/j.cej.2025.170404. URL: https://www.sciencedirect.com/science/article/pii/S1385894725112485.

[17] D. Pallarès. “Fluidized bed combustion - modeling and mixing”. PhD thesis. Göteborg, Sweden: Chalmers University of Technology, 2008. ISBN: 978-91-7385-142-8.

[18] A. Köhler, D. Pallarès, and F. Johnsson. “Modeling Axial Mixing of Fuel Particles in the Dense Region of a Fluidized Bed”. In: *Energy & Fuels* 34.3 (2020), pp. 3294–3304. DOI: 10.1021/acs.energyfuels.9b04194. eprint: https://doi.org/10.1021/acs.energyfuels.9b04194. URL: https://doi.org/10.1021/acs.energyfuels.9b04194.

[19] T. Djerf, D. Pallarès, and F. Johnsson. “Bottom-bed fluid dynamics – Influence on solids entrainment”. In: *Fuel Processing Technology* 173 (2018), pp. 112–118. ISSN: 0378-3820. DOI: https://doi.org/10.1016/j.fuproc.2017.12.023. URL: https://www.sciencedirect.com/science/article/pii/S0378382017311773.

[20] F. Johnsson, S. Andersson, and B. Leckner. “Expansion of a freely bubbling fluidized bed”. In: *Powder Technology* 68.2 (1991), pp. 117–123. ISSN: 0032-5910. DOI: https://doi.org/10.1016/0032-5910(91)80118-3. URL: https://www.sciencedirect.com/science/article/pii/0032591091801183.

[21] B. Leckner. “Fluidization Characteristics of Circulating Fluidized Bed Boilers”. In: *Chemie Ingenieur Technik* 95.1-2 (2023), pp. 32–39. DOI: https://doi.org/10.1002/cite.202200068. eprint: https://onlinelibrary.

wiley.com/doi/pdf/10.1002/cite.202200068. URL: https://onlinelibrary.wiley.com/doi/abs/10.1002/cite.202200068.

[22] T. Djerf, D. Pallarès, and F. Johnsson. "Solids flow patterns in large-scale circulating fluidised bed boilers: Experimental evaluation under fluid-dynamically down-scaled conditions". In: *Chemical Engineering Science* 231 (2021), p. 116309. ISSN: 0009-2509. DOI: https://doi.org/10.1016/j.ces.2020.116309. URL: https://www.sciencedirect.com/science/article/pii/S0009250920308411.

[23] L. Shen, M. Zhang, and Y. Xu. "Solids mixing in fluidized beds". In: *Powder Technology* 84.3 (1995), pp. 207–212. ISSN: 0032-5910. DOI: https://doi.org/10.1016/0032-5910(95)02994-D. URL: https://www.sciencedirect.com/science/article/pii/003259109502994D.

[24] E. Sette et al. "Analysis of Lateral Fuel Mixing in a Fluid-Dynamically Down-Scaled Bubbling Fluidized Bed". In: *Fluidization XIV Conference*. Paper in proceeding. 2013.

[25] R. W. Breault. "A review of gas–solid dispersion and mass transfer coefficient correlations in circulating fluidized beds". In: *Powder Technology* 163.1 (2006). Fluidization and Fluid Particle Systems, pp. 9–17. ISSN: 0032-5910. DOI: https://doi.org/10.1016/j.powtec.2006.01.009. URL: https://www.sciencedirect.com/science/article/pii/S0032591006000167.

[26] T. Djerf, D. Pallarès, and F. Johnsson. "Solids backmixing and entrainment in the splash zone of large-scale fluidized bed boilers". In: *Powder Technology* 404 (2022), p. 117471. ISSN: 0032-5910. DOI: https://doi.org/10.1016/j.powtec.2022.117471. URL: https://www.sciencedirect.com/science/article/pii/S0032591022003655.

[27] F. Johnsson and B. Leckner. "Vertical Distribution of Solids in a CFB-Furnace". In: *Proceedings of the 13th International Conference on Fluidized Bed Combustion*. Orlando, Florida, USA, May 1995.

[28] W. Wu et al. "Radar-based measurement of solids back-mixing in the freeboard of a circulating fluidized bed". In: *Chemical Engineering Journal* 488 (2024), p. 151150. ISSN: 1385-8947. DOI: https://doi.org/10.1016/j.cej.2024.151150. URL: https://www.sciencedirect.com/science/article/pii/S1385894724026378.

[29] W. Wu et al. "Solids separation efficiency at the outlet of a circulating fluidized bed riser". In: *Powder Technology* 428 (2023), p. 118748. ISSN: 0032-5910. DOI: https://doi.org/10.1016/j.powtec.2023.118748. URL: https://www.sciencedirect.com/science/article/pii/S0032591023005326.

[30] T. Djerf et al. "Solids back-mixing in the transport zone of circulating fluidized bed boilers". In: *Chemical Engineering Journal* 428 (2022), p. 130976. ISSN: 1385-8947. DOI: https://doi.org/10.1016/j.cej.2021.130976. URL: https://www.sciencedirect.com/science/article/pii/S1385894721025602.

[31] H. Thunman. *MEN031 Combustion Engineering, Chapter 9: Combustion of Solid Fuels*. Course material. 2020.

[32] R. R. Kumar, A. Kumar Kolar, and B. Leckner. "Shrinkage characteristics of Casuarina wood during devolatilization in a fluidized bed combustor". In: *Biomass and Bioenergy* 30.2 (2006), pp. 153–165. ISSN: 0961-9534. DOI: https:

//doi.org/10.1016/j.biombioe.2005.11.005. URL: https://www.sciencedirect.com/science/article/pii/S0961953405001716.

[33] D.A. da Silva et al. "Volatile matter values change according to the standard utilized?" In: *Research, Society and Development* 10.12 (2021), e291101220476. DOI: 10.33448/rsd-v10i12.20476. URL: http://dx.doi.org/10.33448/rsd-v10i12.20476.

[34] A. Gomez-Barea et al. "Devolatilization of wood and wastes in fluidized bed". In: *Fuel Processing Technology* 91.11 (2010), pp. 1624–1633. ISSN: 0378-3820. DOI: https://doi.org/10.1016/j.fuproc.2010.06.011. URL: https://www.sciencedirect.com/science/article/pii/S037838201000216X.

[35] H. Rezaei et al. "Effects of the mass and volume shrinkage of ground chip and pellet particles on drying rates". In: *Particuology* 38 (2018), pp. 1–9. ISSN: 1674-2001. DOI: https://doi.org/10.1016/j.partic.2017.09.001. URL: https://www.sciencedirect.com/science/article/pii/S1674200117301748.

[36] SciPy Community. *scipy.integrate.solve_ivp*. Accessed: 2026-05-21. 2026. URL: https://docs.scipy.org/doc/scipy/reference/generated/scipy.integrate.solve_ivp.html.

A

Equations to estimate fuel conversion times

Heat-Transfer Correlations and Dimensionless Numbers

Particle Reynolds Number:

$$Re_p = \frac{\rho_g(u_g - u_t)d_p}{\mu_g} \tag{A.1}$$

Correlation for Particle Nusselt Number of Spheres:

$$Nu = 2 + 0.4Re_p^{1/2}Pr^{1/3} \tag{A.2}$$

Convective and Radiant Heat-Transfer Coefficients from Nusselt Number definition and Stefan-Boltzmann law, respectively. The suffix "g" is for gas, "p" for particle:

$$h_{\text{conv}} = \frac{Nu\, k_g}{d_p} \tag{A.3}$$

$$h_{\text{rad}} = \varepsilon\sigma\left(T_g^2 + T_p^2\right)(T_g + T_p) \tag{A.4}$$

Effective Heat-Transfer Coefficient:

$$h_{\text{eff}} = h_{\text{conv}} + h_{\text{rad}} \tag{A.5}$$

Drying

Time to heat the particle to the evaporation temperature:

$$t_{\text{heat}} = \frac{m_p c_p(T_{\text{evap}} - T_{p,0})}{h_{\text{eff}} A_p(T_g - T_{\text{evap}})} \tag{A.6}$$

Time for evaporation at constant temperature, using the latent heat of evaporation. The suffix "w" refers to water:

$$t_{\text{evap}} = \frac{m_w h_{\text{vap}}}{h_{\text{eff}} A_p(T_g - T_{\text{evap}})} \tag{A.7}$$

$$\tau_1 = t_{\text{heat}} + t_{\text{evap}} \tag{A.8}$$

Devolatilisation

Devolatilisation time for a heating-rate-limited process. Kinetic-limited processes apply to smaller particles. A_p refers to the particle surface area, c_p is the particle specific heat, T_v is the devolatilisation temperature:

$$\tau_2 \approx -\frac{m_p c_p}{A_p h_{\text{eff}}} \ln\left(\frac{T_g - T_v}{T_g - T_{p,0}}\right) \tag{A.9}$$

Empirical correlation for devolatilization time using the particle size, d_{vs}, in millimeters, and the bed temperaure in °C:

$$\tau_{2,corr} = 12.08 \times 10^4 \, d_{vs}^{1.44} \, T_{bed}^{-1.61} \tag{A.10}$$

Char Combustion

Shrinking sphere restricted by mass transfer model. Applies for large particles in a hot surrounding [31]. M_c refers to the molar mass of carbon, Ω is the stoichiometric ratio of moles of carbon to moles of oxygen, $C_{O_2,\infty}$ is the oxygen concentration in the circulating gas, and D_{O_2,N_2} is the diffusivity of oxygen.

$$\tau_3 = \frac{\rho_c d_p^2}{8\Omega M_c D_{O_2,N_2} C_{O_2,\infty}} \tag{A.11}$$

B

Density and size calculations for biomass particles

Drying

The size reduction of biomass particles after drying can be expressed as:

$$d_{p,dry} = d_{p,wet}(1 - 0.07) \tag{B.1}$$

$$d_{p,dry} = (20 \text{ mm})(1 - 0.07) = 18.6 \text{ mm}$$

The dry solids mass can be calculated from the moisture content as:

$$m_{dry} = m_{wet}(1 - \text{moisture}) \tag{B.2}$$

Thus, the dry density is defined as:

$$\rho_{dry} = \frac{m_{dry}}{V_{dry}} = 6\frac{(1 - \text{moisture})m_{wet}}{\pi(1 - 0.07)^3 d_{p,wet}^3} = \rho_{wet}\frac{(1 - \text{moisture})}{(1 - 0.07)^3} \tag{B.3}$$

$$\rho_{dry} = 559.45 \text{ kg/m}^3$$

Devolatilisation

A similar procedure is carried out for devolatilisation. An initial size value is calculated without fragmentation for the density calculation.

$$d_{p,char,0} = d_{p,wet}(1 - 0.42) \tag{B.4}$$

$$d_{p,char,0} = 11.6 \text{ mm}$$

The char mass can be calculated from the entire composition as:

$$m_{char} = m_{wet}(1 - \text{moisture})\left(\frac{\text{fixed carbon}}{\text{fixed carbon} + \text{volatiles}}\right) \tag{B.5}$$

The char density can then be written as:

$$\rho_{char} = \rho_{wet}\frac{(1 - \text{moisture})\left(\frac{\text{fixed carbon}}{\text{fixed carbon+volatiles}}\right)}{(1 - 0.42)^3} \tag{B.6}$$

$$\rho_{char} = 307.52 \text{ kg/m}^3$$

The final size of char is then defined as:

$$d_{p,char} = d_{p,char,0}(1 - 0.75) \tag{B.7}$$
$$d_{p,char} = 2.9 \text{ mm}$$

C

Computational implementation details

C.1 Logical Indexing Definitions

The referred indices in Figure 3.2 are defined after the identification of the **ml** layer through the dense bed tracking procedure described in Chapter 3. All of the other indices are defined through logical statements comparing vertical layer positions, h, to the position of layer **ml**, h_{ml}. Thus, the logical statements used for in-mesh indexing are defined as follows.

Layers are denoted with the **db** index if:

$$h < h_{ml} - 1 \tag{C.1}$$

Layers are denoted with the **uml** index if:

$$h = h_{ml} - 1 \tag{C.2}$$

Layers are denoted with the **aml** index if:

$$h = h_{ml} + 1 \tag{C.3}$$

Layers are denoted with the **fb** index if:

$$h_{ml} + 1 < h < H_0 \tag{C.4}$$

Layers are denoted with the **tfb** index if:

$$h = H_0 \tag{C.5}$$

Any other indices are either defined manually or are a subset of one of the groups described above. Indices **ml**, **uml**, **aml**, and **tfb** will always correspond to single layers.

C.2 Cell Areas and Volumes

C.2.1 Layer Heights

The number of coarse cells, n_{coarse}, the number of fine cells, n_{fine}, and the coarse-to-fine layer ratio, R_h, are used, along with the system dimensions, to calculate layer

heights. This calculation divides the system into rectangular layers of constant depth and width. Thus, the layer heights are defined from the following expressions:
Furnace volume:

$$V_f = H_0 \times W_0 \times D_0 = V_{\text{coarse}} + V_{\text{fine}} \tag{C.6}$$

Layer volume:

$$V_l = h_l \times W_0 \times D_0 = V_{\text{annulus}} + V_{\text{core}} \tag{C.7}$$

Fine layer height:

$$h_{\text{fine}} = \frac{V_f}{W_0 D_0 (n_{\text{fine}} + n_{\text{coarse}} R_h)} \tag{C.8}$$

Coarse layer height:

$$h_{\text{coarse}} = h_{\text{fine}} R_h \tag{C.9}$$

C.2.2 Areas and Volumes

The calculation of areas and volumes is based on the diagram shown in Figure C.1. The furnace is assumed to have a rectangular cross-section.

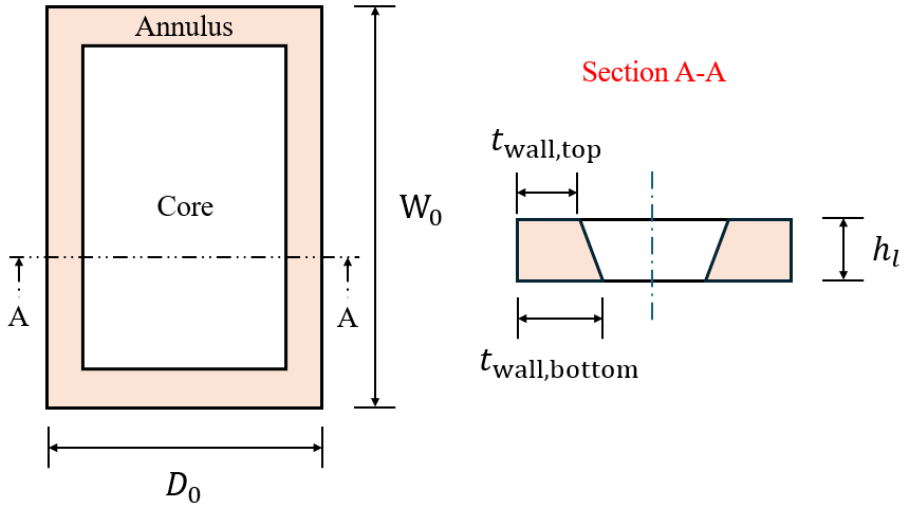

Figure C.1: Furnace cross-section schematic for transport area and volume calculation.

In the top and bottom faces, the depth and width of the core are defined, respectively:

$$W_{\text{core,top}} = W_0 - 2t_{\text{wall,top}} \tag{C.10}$$

$$W_{\text{core,bottom}} = W_0 - 2t_{\text{wall,bottom}} \tag{C.11}$$

$$D_{\text{core,top}} = D_0 - 2t_{\text{wall,top}} \tag{C.12}$$

$$D_{\text{core,bottom}} = D_0 - 2t_{\text{wall,bottom}} \tag{C.13}$$

The areas of the top face of the core and annulus regions are described as:

$$A_{\text{core,top}} = W_{\text{core,top}} \times D_{\text{core,top}} \tag{C.14}$$

$$A_{\text{annulus,top}} = W_0 D_0 - (W_{\text{core,top}} \times D_{\text{core,top}}) \tag{C.15}$$

The areas of the bottom face of the core and annulus regions are described as:

$$A_{\text{core,bottom}} = W_{\text{core,bottom}} \times D_{\text{core,bottom}} \tag{C.16}$$

$$A_{\text{annulus,bottom}} = W_0 D_0 - (W_{\text{core,bottom}} \times D_{\text{core,bottom}}) \tag{C.17}$$

The side area used for the core-to-annulus transport is defined considering the 4 wall layers. This area is taken as the projected rectangular area of the wall layers, such that:

$$A_{\text{side}} = h_l(2D_0 + 2W_0 - 4t_{\text{wall,top}} - 4t_{\text{wall,bottom}}) \tag{C.18}$$

The volume of a truncated pyramid such that describes the volume of the core region of a layer:

$$V_{l,\text{core}} = \frac{1}{3} h_l \times \left(A_{\text{core,bottom}} + A_{\text{core,top}} + \sqrt{A_{\text{core,bottom}} \times A_{\text{core,top}}} \right) \tag{C.19}$$

The volume of the annulus region of a layer is the remaining layer volume:

$$V_{l,\text{annulus}} = V_l - V_{l,\text{core}} \tag{C.20}$$

D

Script Organization

The scripts used for input loading, calculation routines, and post-processing procedures in this work are listed below, with details on what they do and contain:

- **cfb.py**: Main running code. Calls several scripts and organizes the parameters for solving. Has the definition of the ODE system used by *solve_ivp* during time marching.
- **solhydro_funs.py**: Contains the functions developed for calculation routines such as fluidization parameter calculations, dense bed tracking, and transport matrices building, among others. The functions are called by almost all scripts.
- **species.py**: Contains the data classes and initialization functions for the gas and solids species used in the model. All inputs on solids characterization, such as densities, PSDs, etc., are given in this script, along with fuel particle predefined size categories based on shrinkage rates. For the present work, only the solids species were involved.
- **dimensions.py**: Contains the system dimensions class, with information on boiler dimensions and additional calculation routines if necessary.
- **operation.py**: Contains the operating conditions of the system, including gas velocities, maximum solids fraction, and initial bed height. For this work, the gas properties like density and viscosity were also included.
- **fuel.py**: Contains callable functions for **cfb.py** used for fuel injection and conversion source term computation, during time marching.
- **mesh.py**: Contains the mother and son data classes responsible for mesh elaboration, including area and volume calculation. System dimensions are loaded externally. The user specifies the number of coarse layers, fine layers, and coarse-to-fine height ratio directly in this script.
- **cfb_post.py** and **sa.py**: These are post-processing and sensitivity analysis scripts, loading data classes saved from **cfb.py**. **cfb_post.py** mainly contains callable functions to produce relevant plots. **sa.py** produces primarily loads the saved data and produces plots accordingly.

DEPARTMENT OF SOME SUBJECT OR TECHNOLOGY
CHALMERS UNIVERSITY OF TECHNOLOGY
Gothenburg, Sweden
www.chalmers.se

CHALMERS
UNIVERSITY OF TECHNOLOGY